

AMERICAN UNIVERSITY OF BEIRUT

FINITE ELEMENT MODELING OF RAMMED EARTH
CONSTRUCTIONS

by

CHARBEL YAACOUB SALLOUM

A thesis
submitted in partial fulfillment of the requirements
for the degree of Master of Engineering
to the Department of Civil and Environmental Engineering
of the Maroun Semaan Faculty of Engineering and Architecture
at the American University of Beirut

Beirut, Lebanon
August 2024

AMERICAN UNIVERSITY OF BEIRUT

FINITE ELEMENT MODELING OF RAMMED EARTH
CONSTRUCTIONS

by

CHARBEL YAACOUB SALLOUM

Approved by:

Mr. Aram Yeretjian, Assistant Professor
School of Architecture and Design

Advisor

Dr. Mounir Mabsout, Professor
Department of Civil and Environmental Engineering

Co-Advisor

Dr. Shadi Najjar, Professor
Department of Civil and Environmental Engineering

Member of Committee

Date of thesis defense: August 28, 2024

ABSTRACT

OF THE THESIS OF

Charbel Yaacoub Salloum

for

Master of Engineering

Major: Civil Engineering

Title: Finite Element Modeling of Rammed Earth Constructions

Rammed earth has gained popularity due to its environmental impact compared to the traditional ways of construction. Using rammed earth, Soils will be poured into a formwork system and compacted using a hammer to build various systems of different architectural shapes. Once the formwork is totally removed, the system will be susceptible to many loading factors depending on the zoning where it is built (snow load, earthquake loads, wind loads, gravity loads etc...). Also, they produce less emissions of carbon dioxide and therefore more eco-friendly. It is also known that well stabilized rammed earth constructions can be as strong and viable as a conventional structure namely concrete and/or steel materials. Several models including a ruler with concentrated mass load on its tip, a 2D elastic axisymmetric cylinder with top discrete rigid caps, and both elastic and elastoplastic 2D axisymmetric cylinder along with a 3D rammed earth wall of dimensions like those at the American University of Beirut (AUB) confirm that the finite element software ABAQUS is functioning properly. Moreover, rammed earth material is quasi-brittle that could be modeled using the Concrete Damage Plasticity model while assessing the effect of several sizes of square and circular openings at different locations on a typical wall. In addition, stiffer localized effect at the opening surface could work as a reinforcement to prevent sudden failure.

TABLE OF CONTENTS

ABSTRACT	1
ILLUSTRATIONS	5
TABLES.....	9
INTRODUCTION AND BACKGROUND	10
1.1. Background on Rammed Earth Material	11
1.2. Rammed Earth Modeling – Present Status	12
1.3. Research Significance	13
1.4. Research Objectives.....	14
1.5. Thesis Organization	14
BACKGROUND RESEARCH AND CONSTITUTIVE MODELS	15
2.1. Soil Sampling and Composition	15
2.1.1 Methodology	15
2.1.2 Soil Sampling and Experimentation	15
2.1.3 Summary of Findings.....	17
2.2. Rammed Earth Sampling, Testing and Validation	18
2.2.1 Rammed Earth Sampling and Testing	18
2.2.2 Validation.....	21
FINITE ELEMENT ANALYSIS AND VALIDATION	25
3.1. Finite Element Method - General.....	25
3.2. ABAQUS FEM Software Description and Validation	26

3.1.1 2D axisymmetric cylinder with caps (30 cm diameter and 60 cm height)	29
3.1.2 2D axisymmetric cylinder (50cm diameter and 200 cm height).....	35

RAMMED EARTH WALL MODELING 42

4.1. Existing sample wall at AUB of dimensions 1600 mm high, 1000 mm wide, and 400 mm thick.....	42
--	----

4.2. Real size large wall of dimensions 5000 mm length, 2800 mm height, 400mm thickness with 600 mm x 600 mm square opening in the middle.	46
---	----

4.3. Validation for Quarter Rammed Earth Wall of Size 2500 mm wide, 2800 mm high and 200 mm thick, with no openings.....	51
--	----

4.3.1. Case 1: Quarter Wall of Dimensions 2500m*2800m*200mm restrained along x direction on both short width vertical faces.	53
---	----

4.3.2. Case 2: Quarter Wall of Dimensions 2500m*2800m*200mm restrained along x direction on both short width vertical faces with 40cm by 40cm opening in the center.	55
---	----

4.3.3. Case 3: Quarter Wall of Dimensions 2500m*2800m*200mm restrained along x direction on both short width vertical faces with 60cm by 60cm opening in the center.	60
---	----

4.3.4. Case 4: Quarter Wall of Dimensions 2500m*2800m*200mm restrained along x direction on both short width vertical faces with 80cm by 80cm opening in the center.	62
---	----

4.3.5. Case 5: Quarter Wall of Dimensions 2500m*2800m*200mm restrained along x direction on both short width vertical faces with 60cm by 60cm opening located 1/3 from top (a), and 1/3 from bottom surface (b).	65
---	----

4.3.6. Case 6: Quarter Wall of Dimensions 2500m*2800m*200mm restrained along x direction on both short width vertical faces with circular opening of 40cm diameter in the center.	73
--	----

4.3.7. Case 7: Quarter Wall of Dimensions 2500m*2800m*200mm restrained along x direction on both short width vertical faces with circular opening of 60cm diameter in the center.	76
--	----

4.3.8. Case 8: Quarter Wall of Dimensions 2500m*2800m*200mm restrained along x direction on both short width vertical faces with circular opening of 80cm diameter in the center.	79
--	----

4.3.9. Cases 9-10: Quarter Wall of Dimensions 2500m*2800m*200mm restrained along x direction on both short width vertical faces with square opening of 60 cm by 60 cm (Case 9) and circular opening 60 cm diameter (Case 10) square with stiffened teak wood of E=20GPa.	81
---	----

SUMMARY, RECOMMENDATIONS, AND CONCLUSIONS	86
.....	
5.1. Summary	86
5.2. Recommendations	87
5.3. Conclusions	87
REFERENCES	89

ILLUSTRATIONS

Figure

1. The Rammed Earth construction process, as described by Earth & Sun Construction (Gramlich, 2013).....	10
2. Compression Stress-Strain Curve for the Pneumatic Tamper and Proctor Machine (AlKareh, 2020).....	17
3. Optimum Moisture Content.....	20
4. Compression Test Results (Chebeir, 2024).....	20
5. Shear Stress vs Normal Stress (Chebeir, 2024).....	21
6. Cylinder Setup with Applied Displacement Load and Boundary Conditions	22
7. Stress-Strain Curves for CDP, Mohr-Coulomb and Laboratory Testing (Chebeir, 2024).....	24
8. Ruler Tip Displacement.....	28
9. Load and Boundary Conditions.....	30
10. Meshing of the 2D Axisymmetric Cylinder 1	31
11. Stress S22 Result (Main Longitudinal Axial – Uniform).....	31
12. Strain E22 Result (Main Longitudinal Axial – Uniform)	32
13. Stress S11 Result (Secondary Radial – Insignificant).....	32
14. Stress S33 Result (Secondary Circumferential – Insignificant).....	33
15. Displacement U2 Result (Main Longitudinal Axial – Linear).....	33
16. Displacement U1 Result (Secondary Radial – Insignificant).....	34
17. Force-Displacement Curve for 2D Axisymmetric Cylinder 1	34
18. Load and Boundary Conditions Applied.....	36
19. Mesh of 2D Axisymmetric Cylinder 2	36
20. Stress S22 Results for Cylinder 50cmx200cm (Main Longitudinal Axial – Uniform).....	37
21. Stress S11 Results for Cylinder 50cmx200cm (Secondary Radial – Insignificant)	38
22. Stress S33 Results for Cylinder 50cmx200cm (Secondary Circumferential – Insignificant)	38

23. Displacement U2 Results for Cylinder 50cmx200cm (Main Longitudinal Axial – Linear)	39
24. Displacement U2 Results for Cylinder 50cmx200cm (Secondary Radial – Small)	39
25. Force-Displacement Curve for 2D Axisymmetric Cylinder 2	40
26. Stress-Strain Curve for Cylinder 50cmx200cm Under Displacement Load	40
27. Wall Boundary Conditions of AUB Wall Using a Quarter Model	43
28. Meshing of AUB Wall	43
29. Stress S22 Results for AUB Wall (Main Longitudinal Axial – Uniform) ..	44
30. Stress S11 Results for AUB Wall (Secondary Lateral – Practically Zero) ..	44
31. Stress S33 Results for AUB Wall (Secondary Out of Plane – Practically Zero)	44
32. Displacement U2 Results for AUB Wall (Main Longitudinal Axial – Linear)	45
33. Displacement U3 Results for AUB Wall (Secondary Out of Plane – Linear)	45
34. Stress-Strain Curve CDP and Experimental.....	46
35. Full Real Wall (5000x2800x400) with (600x600) opening at the center....	47
36. Stress S22 Results for the Wall (5000x2800x400) with (600x600) Opening at the Center (Main Longitudinal Axial – Uniform)	48
37. Stress S33 Results for the Wall (5000x2800x400) with (600x600) Opening at the Center (Secondary Out of Plane – Insignificant).....	48
38. Stress S11 Results for the Wall (5000x2800x400) with (600x600) Opening at the Center (Secondary Radial).....	49
39. Displacement U1 Results for the Wall (5000x2800x400) with (600x600) Opening at the Center (Secondary Radial – Uniform)	49
40. Displacement U2 Results for the Wall (5000x2800x400) with (600x600) Opening at the Center (Main Longitudinal Axial – Linear).....	50
41. Displacement U3 Results for the Wall (5000x2800x400) with (600x600) Opening at the Center (Secondary Out of Plane – Uniform)	50
42. Quarter Rammed Earth Wall with No Opening.	51
43. Load Displacement P-Delta for Large Wall	52
44. Stress-Strain S22 vs E22 Curve for Large Wall	52

45. Case 1 Model.....	54
46. P-Delta Curve for Case 1.....	55
47. S22 vs E22 for Case 1	55
48. Case 2 Model.....	56
49. Mesh for Case 2.....	57
50. P-Delta Case 2	58
51. P vs S11, S22, S33 at Top of Wall for Case 2.....	58
52. P vs S11, S22, S33 at Top and Bottom of Opening for Case 2.....	59
53. P-Delta for Case 3	61
54. P vs S11, S22, S33 at Top of Wall for Case 3.....	61
55. P vs S11,S22,S33 at Top and Bottom of Opening for Case 3.....	62
56. P-Delta for Case 4	63
57. P vs S11, S22, S33 at Top of Wall for Case 4.....	64
58. P vs S11, S22, S33 at Top and Bottom of Opening for Case 4.....	64
59. Wall with Opening on 1/3 Top Model	65
60. Mesh for Case 5 (a)	66
61. P-Delta for Case 5 (a).....	66
62. P vs S11, S22, S33 at Top of Wall for Case 5 (a).....	67
63. P vs S11, S22, S33 at Top of Opening for Case 5 (a).....	67
64. P vs S11, S22, S33 at Bottom of Opening for Case 5 (a).....	68
65. Wall with Opening on 1/3 Bottom Model.....	69
66. Mesh for Case 5 b.....	70
67. P-Delta for Case 5 (b).....	70
68. P vs S11, S22, S33 at Top of Wall for Case 5 (b).....	71
69. P vs S11, S22, S33 at Top of Opening for Case 5 (b).....	71
70. P vs S11,S22,S33 at Bottom of Opening for Case 5 (b)	72
71. Wall with Circular Opening Case 6	73
72. Mesh for Case 6.....	74
73. P-Delta for Case 6	74

74. P vs S11,S22,S33 at Top of Wall for Case 6.....	75
75. P vs S11, S22, S33 at Top of Opening for Case 6.....	75
76. P vs S11, S22, S33 at Bottom of Opening for Case 6	76
77. P-Delta for Case 7	77
78. P vs S11,S22,S33 at Top of Wall for Case 7.....	77
79. P vs S11,S22,S33 at Top of Opening for Case 7.....	78
80. P vs S11,S22,S33 at Bottom of Opening for Case 7	78
81. P-Delta for Case 8	79
82. P vs S11, S22, S33 at Top of the Wall for Case 8.....	79
83. P vs S11, S22, S33 at Top of the Opening for Case 8.....	80
84. P vs S11, S22, S33 at Bottom of the Opening for Case 8	80
85. P-Delta for Case 9	81
86. P-Delta for Case 10	82
87. P vs S11, S22, S33 at Bottom of Wall for Case 9	82
88. P vs S11, S22, S33 at Top of Wall for Case 10.....	83
89. P vs S11, S22, S33 at Bottom of Opening for Case 9	83
90. P vs S11, S22, S33 at Bottom of Opening for Case 10	84
91. P vs S11, S22, S33 at Top of Opening for Case 9.....	84
92. P vs S11, S22, S33 at Top of Opening for Case 10.....	84

TABLES

Table

1. Suitable Rammed Earth Mix Key Indicators (Burroughs, 2008)	11
2. Mix Composition of Soil with the Addition of Sand (AlKareh, 2020)	15
3. Composition of the 6 Walls (AlKareh, 2020).....	16
4. Compressive Strength Summary for the 6 Samples (AlKareh, 2020).....	17
5. Composition of Samples (Chebeir, 2024).....	18
6. Sample A Final Composition (Chebeir, 2024)	19
7. Sample B Final Composition (Chebeir, 2024).....	19
8. Material Properties (CDP) (Chebeir, 2024)	23
9. Material Properties (Mohr-Coulomb and Drucker-Prager) (Chebeir, 2024)	24
10. Material Properties	37
11. Yield Stress and Plastic Strain Inputs	37

CHAPTER 1

INTRODUCTION AND BACKGROUND

Rammed earth is a material composed of a mix of sandy-clayey gravels, most used for vertical construction but also applicable to floors, roofs, and foundations (Bui et al., 2014; Gramlich, 2013). The structure construction involves layering soil in 10-15 cm parts within a formwork and compacting it until the density and moisture content required are achieved. Once the wall reaches the intended height and the formwork removed, the structure will be strong enough to stand independently (Bui et al., 2014; Nowamooz & Chazallon, 2011). Rammed earth is known for its excellent thermal performance, as demonstrated by historic structures like the Great Wall of China and the Alhambra in Spain (Jiang et al., 2023; Ciancio & Beckett, 2013). The procedure for building rammed earth wall is summarized in Figure 1

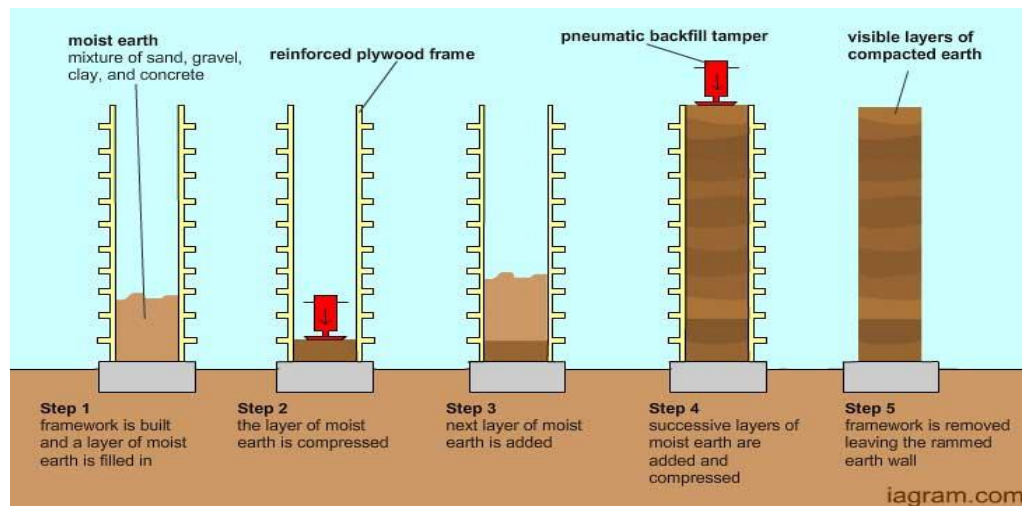


Figure 1 The Rammed Earth construction process, as described by Earth & Sun Construction (Gramlich, 2013)

1.1. Background on Rammed Earth Material

Rammed earth, used since the 7th century B.C., remains valued for its sustainability and cost-effectiveness. It has been employed globally, offering attractive shapes with its horizontal layers (Birznieks, 2013) and sheltering more than half of the world's population (Avrami, 2008).

There are two types of rammed earth material; non-stabilized and stabilized (El Nabouch et al., 2015). Its environmental benefits include low energy use and minimal waste (Librici, 2016). It uses only 1% of the energy of reinforced concrete (Avila et al., 2020), and its low energy content further enhances its environmental advantage (Consoli et al., 2022).

Rammed earth also is efficient for noise reduction, fire resistance and insulation due to its high thermal mass (Lovec et al., 2018). Economically, it lowers material and transportation costs, though labor costs remain similar or close to concrete constructions. Construction costs can be 60% lower compared to concrete (Avila et al., 2020).

Burroughs (2008) reviewed various studies on rammed earth and identified a suggestion on the findings (Alkareh, 2020). The percentages of appropriate mix are shown in Table 1

Table 1 Suitable Rammed Earth Mix Key Indicators (Burroughs, 2008)

Indicator	Value
Clay	5-25%
Clay/Silt	30-35%
Plasticity Index (PI)	<15%
Linear Shrinkage (LS)	<6%

Sieve and hydrometer tests are used to analyze soil samples. If the recommended range is exceeded, the addition of sand can help reduce the clay content and achieve the suitable mix (Alkareh, 2020). The Standard or Modified Proctor test, as described in ASTM D698 (2012), is used to determine the optimal moisture content and corresponding dry density. The optimum moisture content is at the maximum of the curve.

Knowledge of soil mechanical properties to accurately modeling rammed earth walls is required which can be uncertain due to soil variability (Silva et al., 2014). Key indicators influencing strength include moisture content, grain size, compaction, additives, and fiber content. Literature provides density values between 1,700 and 2,400 kg/m³ (Librici, 2016) and compressive strength between 1.5 and 4.0 N/mm (El Nabouch et al., 2015). It is crucial to balance complexity, reliability, and accuracy for numerical modeling (Miccoli et al., 2014).

1.2. Rammed Earth Modeling – Present Status

Finite element modeling (FEM) of these walls, especially their non-linear behavior, is still limited in the literature. It is crucial to accurately model the non-linear behavior to understand the seismic performance of rammed earth walls, which experience large deformations (Miccoli et al., 2014). Almost all existing models are simplified, assuming linear isotropic and elastic-perfectly plastic behavior, without capturing the material's true non-linear characteristics (Miccoli et al., 2014). Advanced FEM software like ABAQUS/CAE offers non-linear capabilities for more accurate simulations. It also supports contact modeling, making it extremely useful for simulating layered structure of rammed earth (Solan, 2019).

1.3. Research Significance

Scientists are seeking ways to reduce CO₂ emissions, with the construction industry responsible for high percentage of global emissions playing a critical role in sustainable development (Chen et al., 2021). Rammed earth has gained attention in recent years due to its low environmental impact (Avila et al., 2022). Rammed earth offers significantly lower energy footprint throughout its lifecycle, from construction to demolition (El Nabouch et al., 2015).

Despite its benefits, there is limited research on modeling rammed earth as a conventional building material like concrete and steel. This research aims to develop an approach to model rammed earth using the finite element software ABAQUS.

Numerical modeling is important for evaluating the behavior of rammed earth structures where it helps engineers understand structural behavior, failure mechanisms, and optimization strategies for rammed earth structures.

Additionally, numerical modeling enables the study of more complex designs, such as wall openings, corners, and multi-story buildings, and provides ways to optimize and enhance structural performance. It also allows for the examination of variables like wall thickness, soil composition, and the use of additives, which is essential for reducing waste and construction costs.

1.4. Research Objectives

Given the Concrete Damage Plasticity Model as the accurate model to simulate the full behavior of rammed earth material, the work is divided into several objectives.

The first objective is to understand how ABAQUS works by performing several validations for typical simple models to more complex ones.

The second objective is to simulate the existing AUB Rammed Earth Wall using the Concrete Damage Plasticity model and check whether the stress strain data obtained are similar to that of the 2D Axisymmetric Cylinder studied concurrently by Chebeir (2024).

The third and final objective is to assess the failure behavior of a typical wall with different cases of square and circular openings by analyzing the total force applied on the top surface versus the displacements and versus the stresses at different locations.

1.5. Thesis Organization

The first chapter provides introduction and background information on rammed earth including numerical modeling, research significance and objectives. The second chapter describes the background research and the constitutive models on rammed earth construction conducted by AlKareh (2020) at the American University of Beirut (AUB) and concurrently the sampling, testing and validation of models by Chebeir (2024). The third chapter includes finite element analysis and validation. The fourth chapter presents rammed earth wall modeling with different opening cases. The last chapter contains the summary, recommendations, and conclusions.

CHAPTER 2

BACKGROUND RESEARCH AND CONSTITUTIVE MODELS

2.1. Soil Sampling and Composition

Sampling and testing at the American University of Beirut (AUB) conducted by AlKareh (2020) is discussed in the following sections

2.1.1 Methodology

AlKareh's (2020) goals were to assess soil suitability, develop standards for future research, build sample walls in two different locations, and check their thermal performance. Two sets of six walls were constructed using the same soil from AUB's Advancing Research and Enabling Communities (AREC). One set was built at AREC in the arid Beqaa Valley, and the other on AUB's campus in Beirut, which has a wet climate.

2.1.2 Soil Sampling and Experimentation

To assess the AREC soil, sieve analysis, hydrometer analysis, and Atterberg limits were tested. The high clay content required sand to be added, resulting in the final composition shown in Table 2

Table 2 Mix Composition of Soil with the Addition of Sand (AlKareh, 2020)

Constituents	Percent by Weight
Gravel	17.5
Sand	35.3
Silt	26.7
Clay	20.6
Total	100

The compositions of the six walls are shown in Table 3.

Table 3 Composition of the 6 Walls (AlKareh, 2020)

Wall	Composition
1	Soil Only
2	75% Soil + 25% Sand
3	75% Soil + 25% Sand + 1 % Cement + 1% Lime
4	75% Soil + 25% Sand + 5% Cement
5	75% Soil + 25% Sand + 5% Lime
6	75% Soil +25% Sand + 4% Cement + 4% Lime

Pneumatic Tamper and Proctor Machine were used to evaluate the structural behavior and performance of the samples. The results showed that the Pneumatic Tamper increased density by 12% and strength by 148% compared to the Proctor Machine (50 blows). The average compressive strength using the Pneumatic Tamper was 1.49 MPa, with an average density of 1,990 kg/m³. The stress-strain curves obtained are shown in Figure 2.

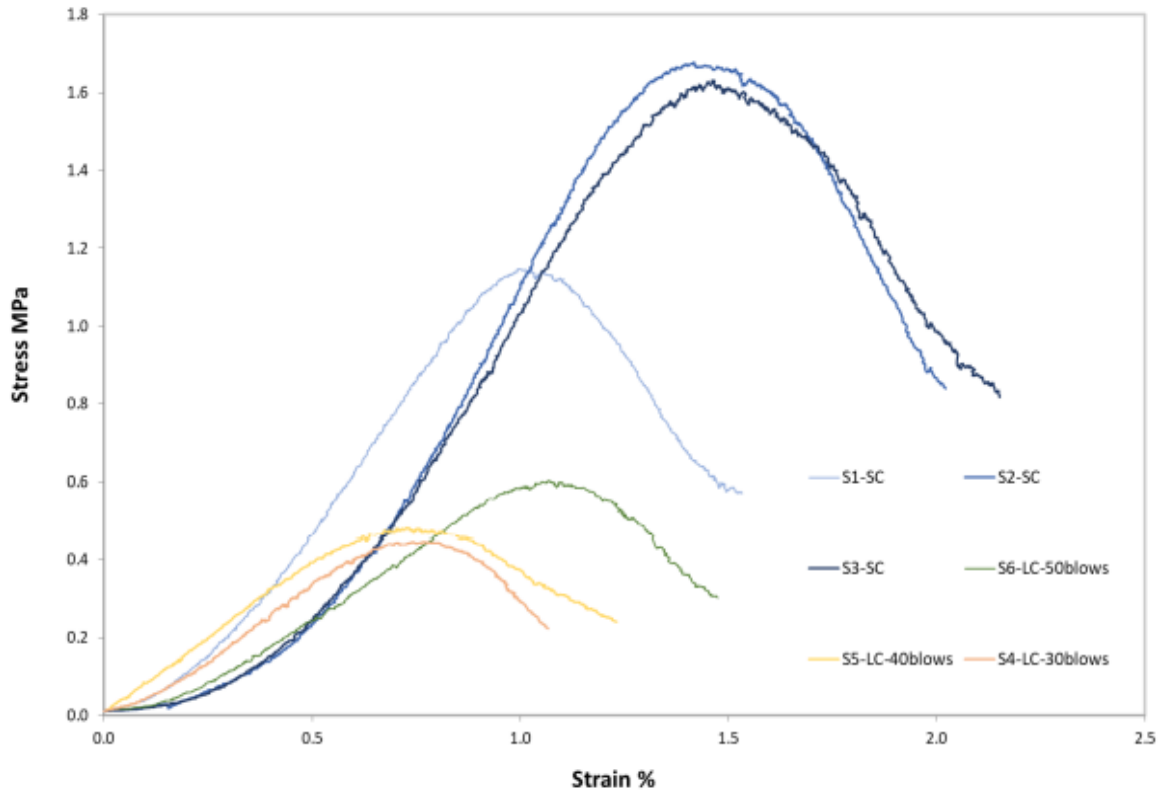


Figure 2 Compression Stress-Strain Curve for the Pneumatic Tamper and Proctor Machine (AlKareh, 2020)

For the six different mixes, adding sand increased strength around 30%, while the 4% lime and 4% cement further boosted strength by 40% compared to using sand alone. The compressive strength data is summarized in Table 4.

Table 4 Compressive Strength Summary for the 6 Samples (AlKareh, 2020)

Mix	Pure Soil	Soil + Sand – Compression Strength f'_c (MPa)				
		Soil + Sand	1% Lime + 1% Cement	4% Lime + 4% Cement	5% Lime	5% Cement
Max f'_c	1.68	2.03	2.07	3.42	1.29	2.21
Average f'_c	1.94	1.94	1.73	2.69	1.21	1.93

2.1.3 Summary of Findings

Two sets of six walls were constructed using soil from AREC: one set in the humid Beirut campus and the other in the arid Beqaa Valley. To assess soil suitability, sieve

analysis, hydrometer analysis, and Atterberg limits were performed. Initially, the high clay content did not meet standards, so sand was added to the mix. Compression strength tests with Pneumatic Tamper and Proctor Machine showed that Pneumatic Tamper significantly improved soil strength and density. Adding sand increased strength by 30%, and incorporating 4% lime and 4% cement boosted it by 40%. Failures were brittle. Although the Standard Proctor Test (SPT) is typically used for optimal water content, a ball drop test was employed in this study.

2.2.Rammed Earth Sampling, Testing and Validation

Sampling, Testing and Validation is done concurrently by Chebeir (2024). Several tests were made in the lab like the modified proctor test, compression test and direct shear test on five samples from Ghaze in Bekaa, Lebanon. Also, three different finite element models were used to validate the stress-strain diagram obtained from the lab.

2.2.1 Rammed Earth Sampling and Testing

Atterberg Limit is conducted on those samples and it is obtained that three of these samples had similar composition and same for the remaining two. The composition of the samples is summarized in Table 5

Table 5 Composition of Samples (Chebeir, 2024)

Composition	Sample 1	Sample 2	Sample 3	Sample 4	Sample 5
Sand	14%	15%	10%	6%	8%
Silt	36%	38%	40%	41%	40%
Clay	50%	47%	50%	53%	52%

The composition of samples 1, 2, and 3 is similar, while the composition of samples 4 and 5 is similar to each other.

The above results do not meet Burrough's recommended values. This suggests the need of adding sand to reduce clay content (Chebeir, 2024).

The final composition of sample A which is the combination of samples 1,2 and 3 and sample B which is the combination of samples 4 and 5 is stated in Table 6 and Table 7

Table 6 Sample A Final Composition (Chebeir, 2024)

Sample A	
Sand	57.0%
Silt	19.0%
Clay	24.0%

Table 7 Sample B Final Composition (Chebeir, 2024)

Sample B	
Sand	54.0%
Silt	20.0%
Clay	26.0%

Atterberg limit test shows that the plasticity index falls below 15 as recommended (Chebeir, 2024). Modified Proctor test resulted in optimum moisture content of 10.2% for a dry density of 2.04 g/cm³ as shown in Figure 3

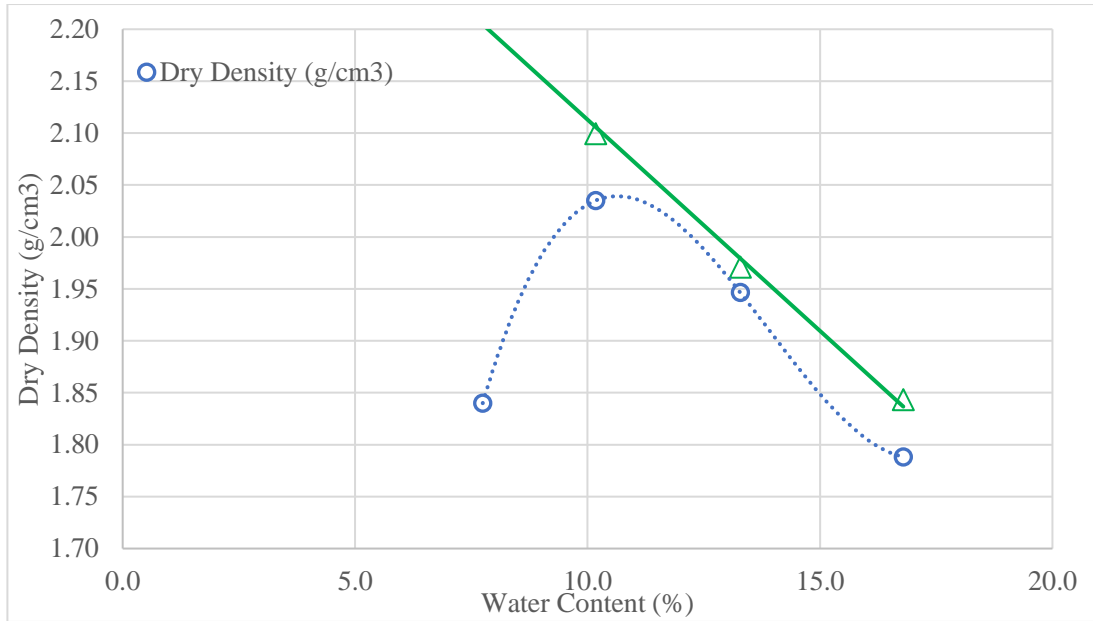


Figure 3 Optimum Moisture Content

Compression test is done by (Chebeir, 2024) on three samples of size 20 cm in height and 10 cm in diameter. The stress-strain curve for the three samples is shown in Figure 4

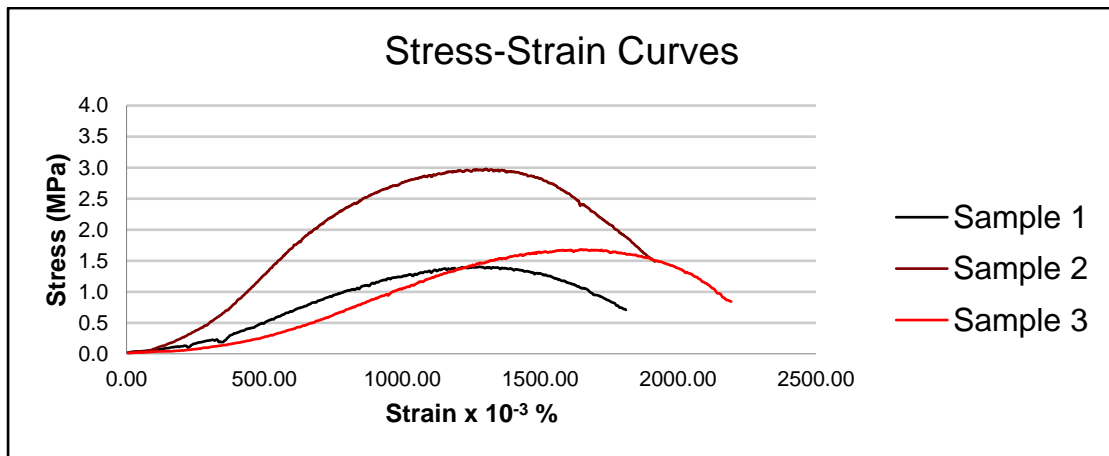


Figure 4 Compression Test Results (Chebeir, 2024)

Sample 2 is disregarded and the average of Sample 1 and 3 is used with an average yield strength of 1.54 MPA.

To determine the cohesion and friction angle of Sample A, Direct Shear test is performed on small sample from a fourth cylinder having the same parameters and characteristics are those used in the compression test. The obtained cohesion is 248.1 KPa and the friction angle is 69.032 degrees.

Figure 5 shows the best fit line equation.

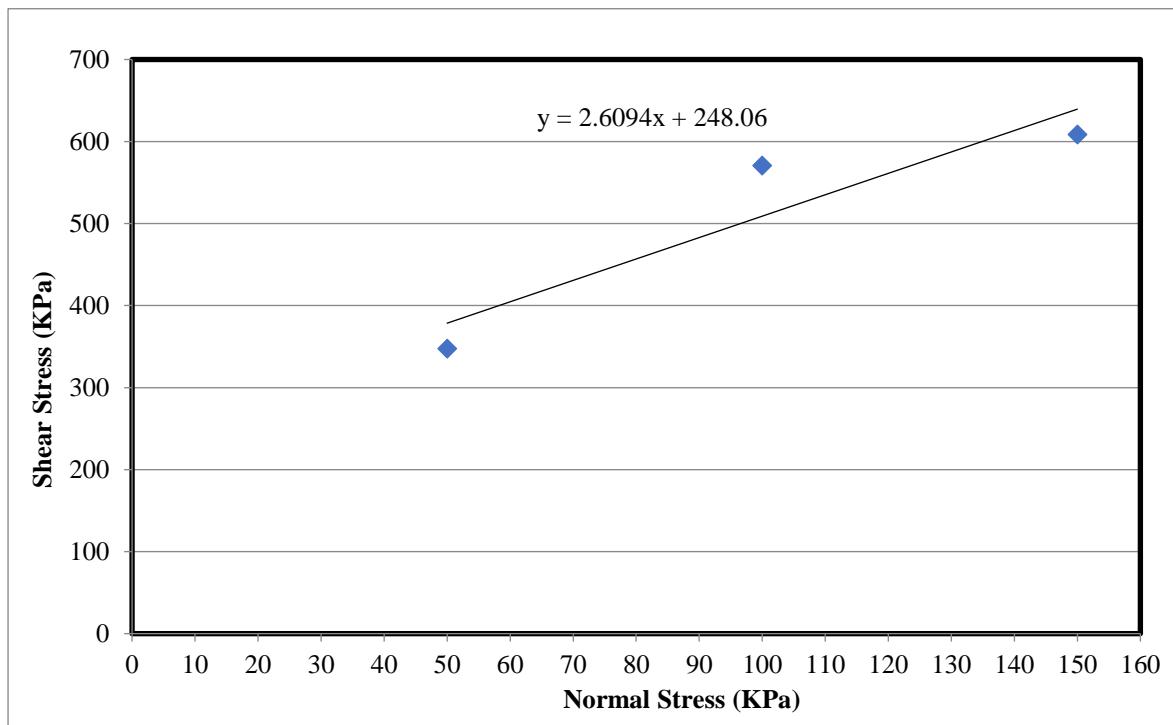


Figure 5 Shear Stress vs Normal Stress (Chebeir, 2024)

2.2.2 Validation

Validation of the Stress-Strain curve in Figure 4 is done concurrently by Chebeir (2024). The author used three different material behavior models to validate the results; Mohr-Coulomb, Drucker-Prager and Concrete Damage Plasticity CDP.

Figure 6 shows the 2D Axisymmetric Cylinder

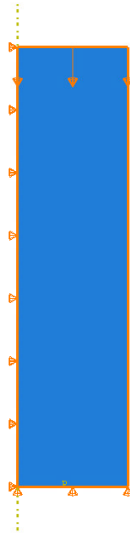


Figure 6 Cylinder Setup with Applied Displacement Load and Boundary Conditions

Material properties for the CDP, Mohr-Coulomb and Drucker-Prager models are listed in Table 8 and Table 9.

Table 8 Material Properties (CDP) (Chebeir, 2024)

Modulus of Elasticity (MPA)	73 (obtained from lab test)
Poisson's Ratio	0.3
Dilation Angle (deg)	30 (typically between 30 and 40) (Lubliner et al, 1989; Lee & Fenves, 1998)
Eccentricity	0.1 (Lubliner et al, 1989) (Lee & Fenves, 1998)
Fb0/fc0	1.16 This is the ratio of the strength of concrete under biaxial compression to the strength under uniaxial compression. Typical values range from 1.1 to 1.16 for normal strength concrete. (Bui et al., 2016) (Lubliner et al., 1989) (Lee & Fenves, 1998)
Kc	0.6667 This is the yield surface shape. (Lubliner et al, 1989) (Lee & Fenves, 1998)
Viscosity Parameter	0
Mesh (5mm Size)	CAX8R An 8-node biquadratic axisymmetric quadrilateral, reduced integration

Table 9 Material Properties (Mohr-Coulomb and Drucker-Prager) (Chebeir, 2024)

Angle of Friction	69 (obtained from lab test)
Dilation Angle	30
Flow Stress Ratio	1 (yield stress in triaxial tension/yield stress in triaxial compression. Average value between 1 and 1.2)
Cohesion	248 KPa (Obtained from lab testing)
Mesh (5mm Size)	CAX8R An 8-node biquadratic axisymmetric quadrilateral, reduced integration

The Stress Strain data resulted from the three different materials ABAQUS Modeling is shown in Figure 8.

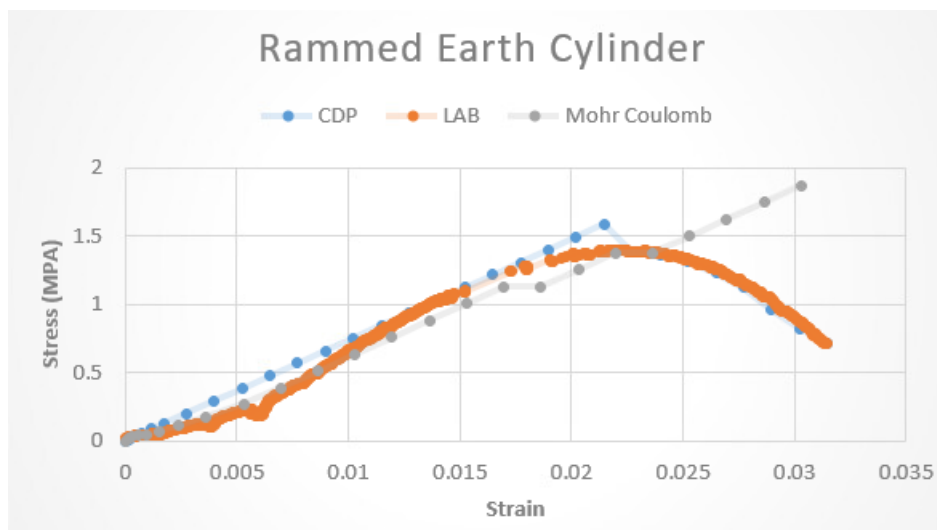


Figure 7 Stress-Strain Curves for CDP, Mohr-Coulomb and Laboratory Testing (Chebeir, 2024)

Chebeir (2024) stated to use the CDP model for rammed earth material since it simulates the full behavior including the softening branch.

CHAPTER 3

FINITE ELEMENT ANALYSIS AND VALIDATION

3.1. Finite Element Method - General

The Finite Element Method (FEM) is a computational technique used to approximate solutions for complex engineering problems governed by differential equations. It involves simplifying and discretizing the problem domain into smaller, simpler finite elements connected at nodes (Nikishkov, 2004). For each element, equations based on the governing differential equations are derived, and these are assembled into a larger system that represents the entire problem. Boundary conditions are applied to this system, and numerical methods solve the resulting equations to find approximate values of the unknown variables at the nodes like displacement, stresses and strains. FEM is versatile and highly accurate, making it suitable for structural analysis, thermal analysis, fluid dynamics, and electromagnetic analysis. Despite its computational intensity and the challenge of mesh generation, FEM is widely used in engineering disciplines, supported by various software tools like ANSYS, ABAQUS, and COMSOL Multiphysics (Sarkar et al., 2022).

In the Finite Element Method (FEM), the mesh is critical for ensuring accuracy, convergence, and computational efficiency. The mesh divides the problem domain into smaller elements, allowing complex geometries and material properties to be approximated accurately. Mesh quality directly impacts the precision of the solution, with finer meshes providing more detailed approximations but at a higher computational cost (Wördenweber, 1984). Mesh types vary, including triangular and tetrahedral elements for flexible meshing of complex shapes, and quadrilateral and hexahedral elements for structured, regular geometries. Additionally, meshes can be

uniform, with elements of similar size, or non-uniform, with variable element sizes to capture local variations more effectively. The choice of mesh type and refinement level is crucial for achieving a balance between accuracy and computational resources in FEM analyses. Mesh Sensitivity analysis for cylinder and walls was studied and showed that mesh sizes 50mm and 100mm are providing similar output results.

3.2.ABAQUS FEM Software Description and Validation

ABAQUS offers various modeling approaches, including 3D models for comprehensive analyses, 2D planar models for plane stress and strain conditions, axisymmetric models for rotationally symmetric structures, shell models for thin-walled structures, beam models for slender structures, membrane models for in-plane force analysis, and solid models for detailed stress and strain information (Manual, A. S. U. S., 2012). Specifically, axisymmetric models simplify the analysis of rotationally symmetric structures by reducing the problem to a two-dimensional representation, significantly lowering computational cost and time while simplifying the modeling and meshing process.

In structural analysis and testing, force vs. displacement control refers to two distinct methods for studying material or structural behavior under loading. **Force control** involves incrementally increasing the applied load and measuring the resulting displacement. This method is useful when the primary focus is on load-bearing capacity, but it can be less effective in capturing the complete structural response, especially in cases of unstable post-peak behavior, where sudden failure may occur. **Displacement control**, on the other hand, involves incrementally increasing displacement and measuring the corresponding force. This approach is often preferred when the goal is to capture the full force-displacement curve,

including post-peak and softening behavior. Displacement control provides a more stable response, making it valuable for understanding failure mechanisms and material performance under increasing deformation. The choice between these methods depends on the specific objectives of the analysis and the expected behavior of the material or structure under load.

First, to validate that the results obtained in theory are the same as on ABAQUS, several “simple” classical models were prepared and tested using linear elastic, small displacement and deformation analysis:

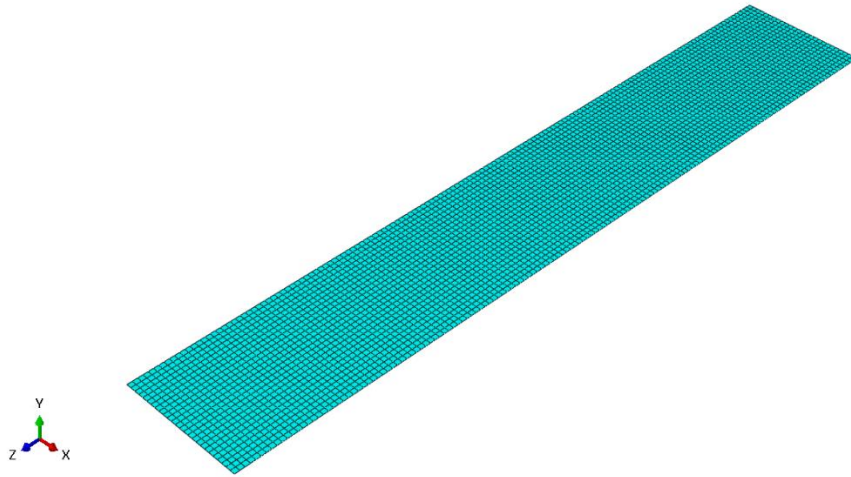
- Fixed-fixed beam with distributed load.
- Fixed-free beam with load at the tip.
- Beam-column steel frame.
- Column under axial load.

For simplicity, a ruler with the following properties was modeled:

- 150mm*26mm*0.7mm
- Modulus of Elasticity $E=193$ GPa

The ruler is restrained at one end and holding a weight of $P=4.46$ N from the other end. It is a typical cantilever beam with concentrated load at the tip having a tip displacement of $PL^3/3EI$ which is equal to 34.98 mm using classical flexure beam theory.

Ruler Mesh: Mesh size 1mm. S8R: An 8-node doubly curved thick shell, reduced integration



The result obtained in ABAQUS result for tip displacement is shown in Figure 8:

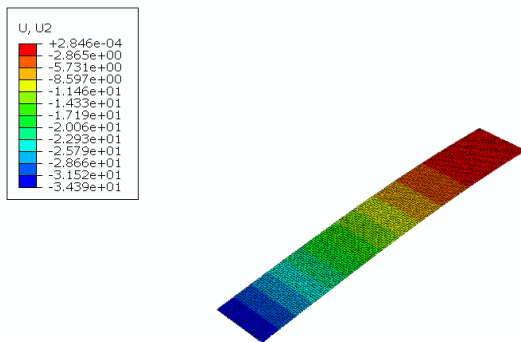


Figure 8 Ruler Tip Displacement

ABAQUS resulted in a displacement of value 34.39 mm which showed a similar calculated result.

Several cylinders were prepared and modeled in order to validate the outputs.

3.1.1 2D axisymmetric cylinder with caps (30 cm diameter and 60 cm height)

Modeling an axisymmetric cylinder in ABAQUS with dimensions 30 cm in diameter and 60 cm in height under various loading cases (concentrated load, pressure load and displacement load), with specific boundary conditions, involves several key steps.

1. Define the model as axisymmetric and sketch the cylinder's side section—a rectangle of 15 cm (radius) by 60 cm (height).
2. Assign the material properties and section definition as axisymmetric.
3. Apply boundary conditions: pin the middle bottom node to prevent translation up and down and restrain both the left and right translations of the top and bottom edges.
4. Apply loads:
 - Pressure load on the inner or outer curved surface by specifying the pressure magnitude
 - Displacement load by prescribing displacement boundary conditions along the top edge
 - Concentrated load by selecting the top center node and defining the load magnitude.
5. Mesh the model using axisymmetric quadrilateral elements (e.g., CAX4R), ensuring finer mesh near load applications and constraint regions for accuracy.
6. Set up and run the analysis, interpret the results for each loading scenario.

The first axisymmetric linear elastic cylinder ($E=200\text{GPA}$ and $\text{Poisson} = 0$) under study was subjected to displacement load of 4 mm in magnitude. The load and boundary conditions are shown in Figure 9:

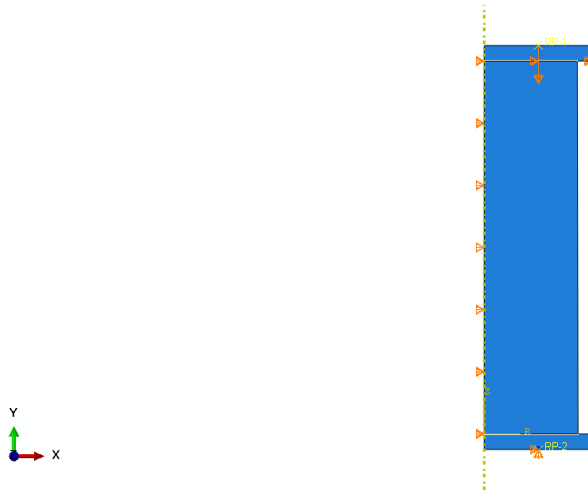


Figure 9 Load and Boundary Conditions

A mesh size of 10 mm and of type CAX4R a 4-node bilinear axisymmetric quadrilateral reduced integration, hourglass control is used for the first cylinder (shown in Figure 10). The results extracted from ABAQUS in terms of stresses (S), strains (E), and displacements (U) in directions 1, 2, and 3 are shown in Figure 11 to Figure 16.

Note that directions 1 (or 11), 2 (or 22), 3 (or 33) indicate radial, longitudinal axial, and circumferential, respectively.

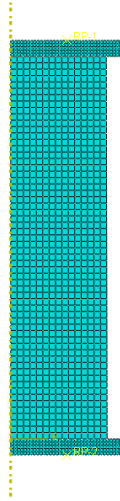


Figure 10 Meshing of the 2D Axisymmetric Cylinder 1

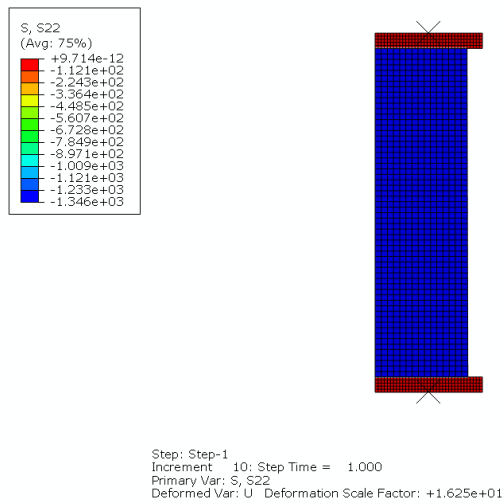


Figure 11 Stress S22 Result (Main Longitudinal Axial – Uniform)

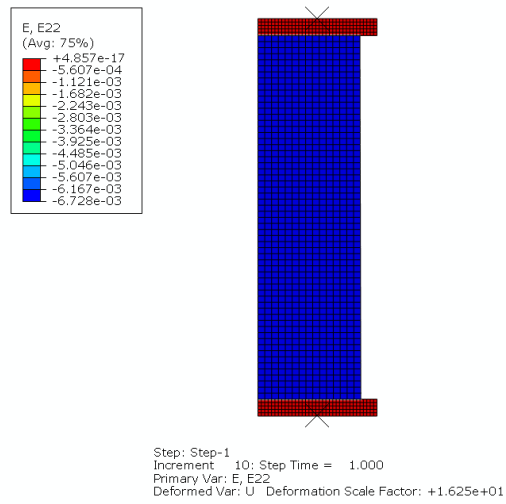


Figure 12 Strain E22 Result (Main Longitudinal Axial – Uniform)

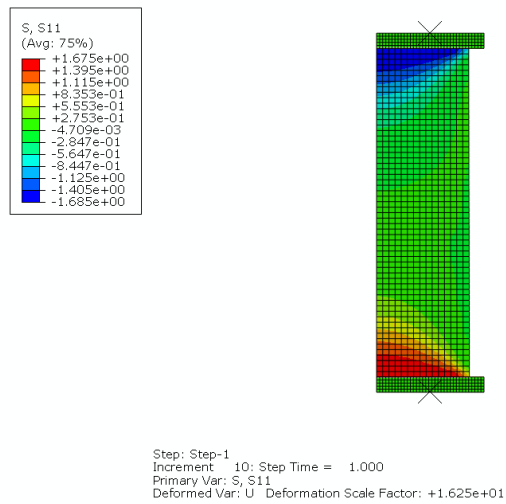


Figure 13 Stress S11 Result (Secondary Radial – Insignificant)

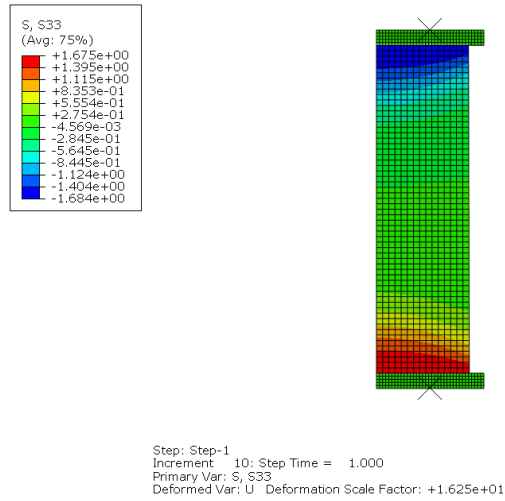


Figure 14 Stress S33 Result (Secondary Circumferential – Insignificant)

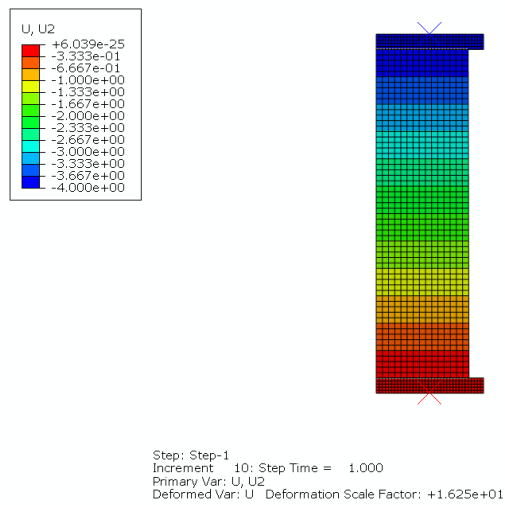


Figure 15 Displacement U2 Result (Main Longitudinal Axial – Linear)

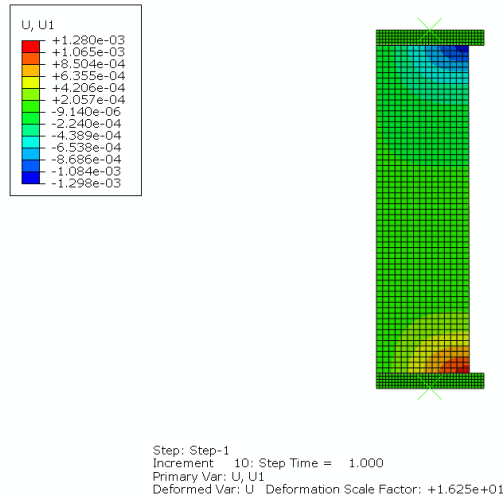


Figure 16 Displacement U1 Result (Secondary Radial – Insignificant)

The force-displacement curve is shown below in Figure 17.

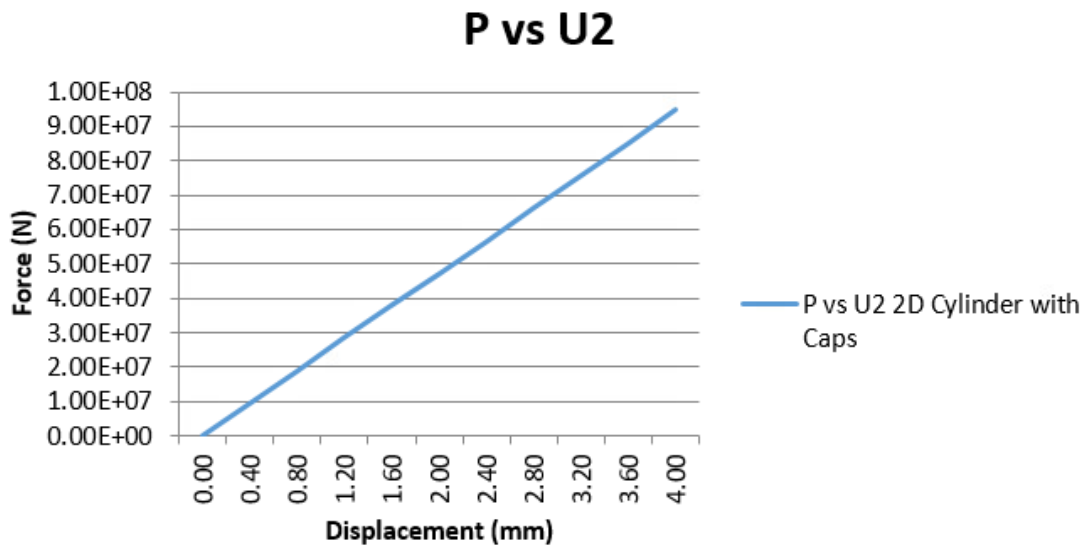


Figure 17 Force-Displacement Curve for 2D Axisymmetric Cylinder 1

As per linear analysis and structural engineering formula $u=PL/AE$ (Beer et al., 1999) where u is the displacement in mm, P is the concentrated load, A is the cross-section area of the cylinder and E is the modulus of Elasticity. Doing calculation while using $\alpha= 4\text{mm}$ we get $S22=1,333.33 \text{ MPa}$ which is very close to the

values obtained in Figure 11 above. This is also applicable for E22 results in Figure 12.

The second axisymmetric linear elastic cylinder ($E=200\text{GPA}$ and $\text{Poisson} = 0$) under study was subjected to a concentrated load of magnitude 94,200 KN. The results obtained are the same as the above ones when a displacement load is applied.

The third axisymmetric linear elastic cylinder ($E=200\text{GPA}$ and $\text{Poisson} = 0$) under study was subjected to a pressure load of magnitude 1,333.33 MPa. The results obtained are the same as the above ones when a displacement load is applied.

3.1.2 2D axisymmetric cylinder (50cm diameter and 200 cm height)

To validate the above results without the use of caps and using the parameters obtained in the laboratory, a 2D axisymmetric cylinder of 50 cm diameter and 200 cm height was modeled, where the model is no longer an “elastic” case, but a “plastic” case.

The cylinder shape under the application of loads and boundary conditions is shown in Figure 18, and the meshing is shown in Figure 19.

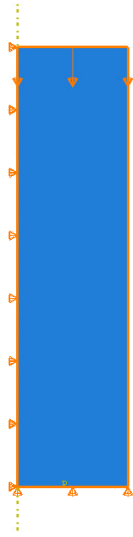


Figure 18 Load and Boundary Conditions Applied

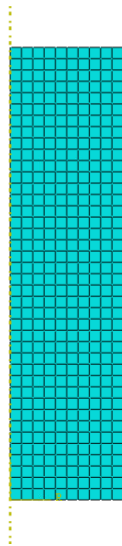


Figure 19 Mesh of 2D Axisymmetric Cylinder 2

The cylinder is restrained in the x direction, pinned at the left bottom edge and restrained in the y direction at the bottom surface.

The material properties used are summarized in Table 10 and Table 11.

Table 10 Material Properties

Modulus of Elasticity	73 MPA
Poisson's Ratio	0.3
Mesh	CAX4R: A 4-node bilinear axisymmetric quadrilateral, reduced integration, hourglass control

Table 11 Yield Stress and Plastic Strain Inputs

Yield Stress (MPA)	Plastic Strain
2	0
4	0.06

A displacement load of 38.7 mm is applied uniformly along the top surface.

The Results for S22, S11, S33, U2 and U1 are shown in Figure 20 to Figure 24 respectively:

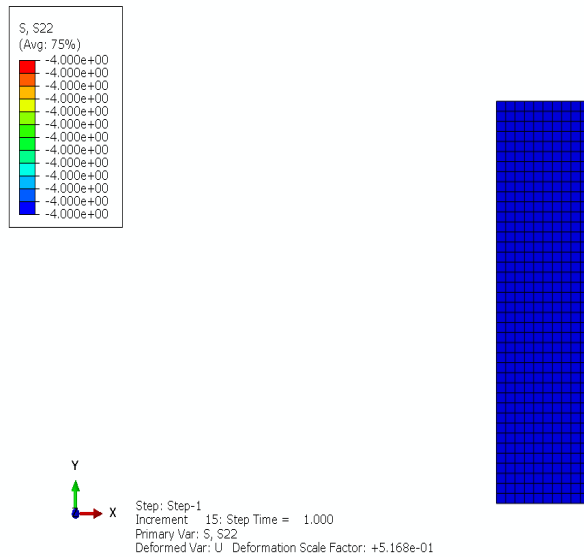


Figure 20 Stress S22 Results for Cylinder 50cmx200cm (Main Longitudinal Axial – Uniform)

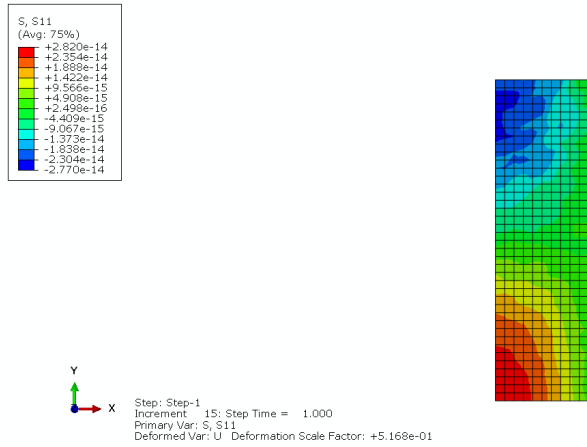


Figure 21 Stress S11 Results for Cylinder 50cmx200cm (Secondary Radial – Insignificant)

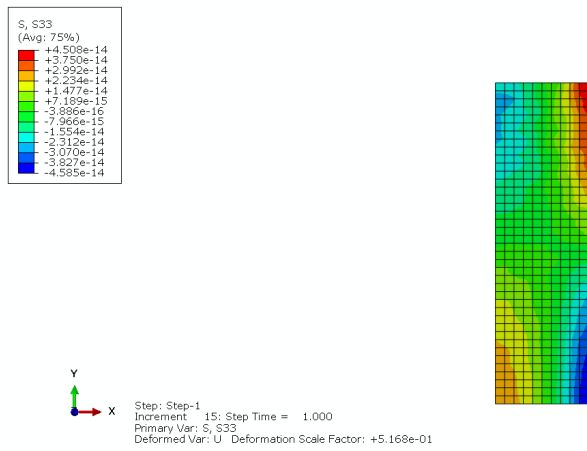


Figure 22 Stress S33 Results for Cylinder 50cmx200cm (Secondary Circumferential – Insignificant)

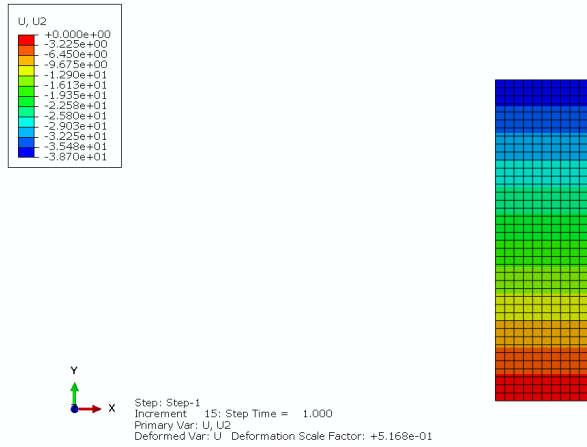


Figure 23 Displacement U2 Results for Cylinder 50cmx200cm (Main Longitudinal Axial – Linear)

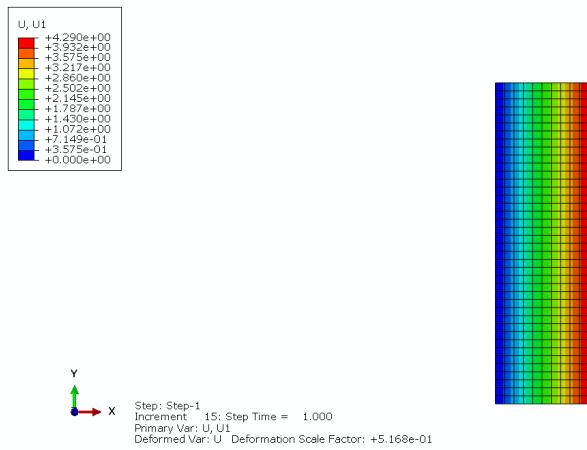


Figure 24 Displacement U2 Results for Cylinder 50cmx200cm (Secondary Radial – Small)

The Force vs Displacement Elastoplastic curve is shown below in Figure 25.

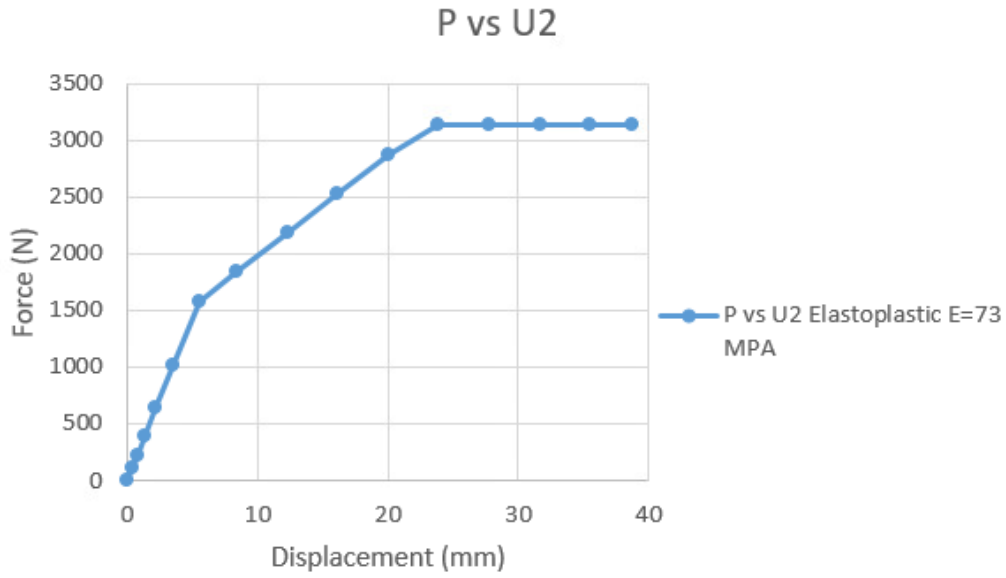


Figure 25 Force-Displacement Curve for 2D Axisymmetric Cylinder 2

The stress-strain curve obtained for Cylinder 50cmx200cm Under Displacement Load is shown in Figure 26.

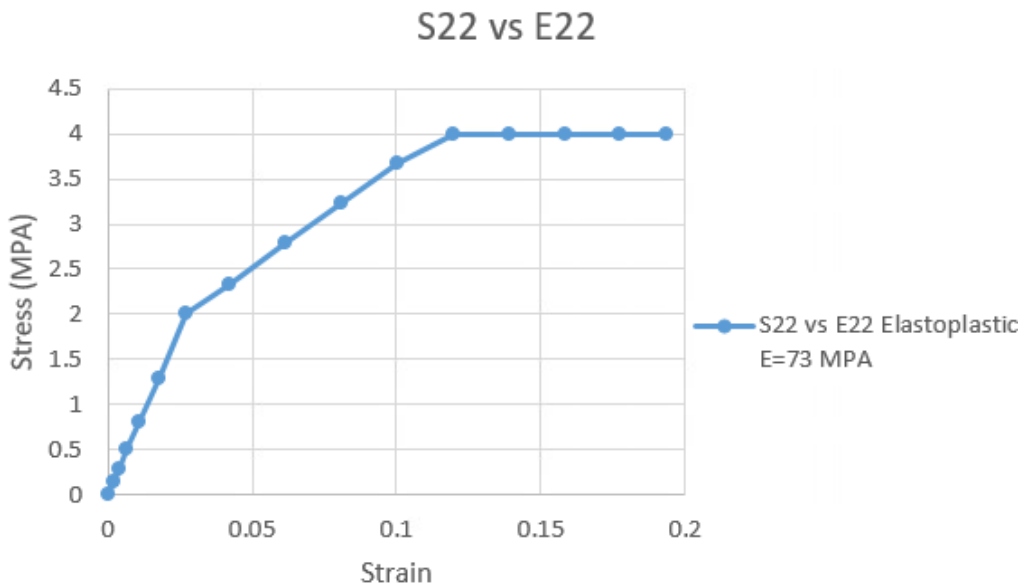


Figure 26 Stress-Strain Curve for Cylinder 50cmx200cm Under Displacement Load

The results obtained show the majority of the stress is borne by S22 with negligible differences in S11 and S33 (on the order of -14). Similarly, for the displacement, the displacement applied is predominant by direction 2 which is consistent with the applied boundary conditions.

CHAPTER 4

RAMMED EARTH WALL MODELING

After validating that the ABAQUS modeling for the cylinders tested using CDP nonlinear material model for rammed earth match the experimental results, the following walls were modeled using the Ghazze rammed earth material:

4.1.Existing sample wall at AUB of dimensions 1600 mm high, 1000 mm wide, and 400 mm thick.

First the stress on the wall is calculated by dividing the compression forces applied to the cross-sectional area of the wall. Then a ratio is obtained by dividing the strain in the wall by the strain in the cylinder. After preparing the stress-strain curves, these curved were inputted into ABAQUS in the compression CDP behavior. The same material properties as in Table 8 were inserted into the model.

Due to biaxial symmetry, a quarter of the wall (500mm*1600mm*200mm) is modeled in ABAQUS with the boundary conditions stated below:

- Pinned over the centerline that joins the quarter of this wall with the other parts.
- Rollers all over the bottom surface except the centerline.
- Restrained in the direction in contact with the other parts.

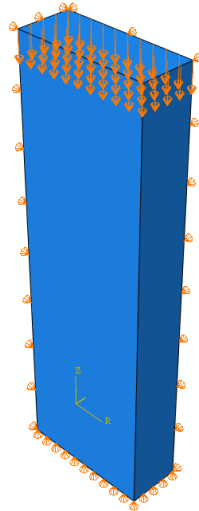


Figure 27 Wall Boundary Conditions of AUB Wall Using a Quarter Model
The mesh used is C3D8R an 8-node linear brick, reduced integration, hourglass control, and is shown in Figure 28.

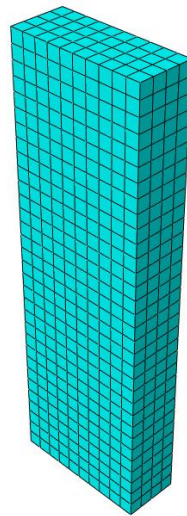


Figure 28 Meshing of AUB Wall

After running the model, the results obtained are shown in Figure 29 to Figure 33.

Note that directions 1 (or 11), 2 (or 22), 3 (or 33) indicate lateral along the width, longitudinal axial, and out-of-plane along the thickness, respectively.

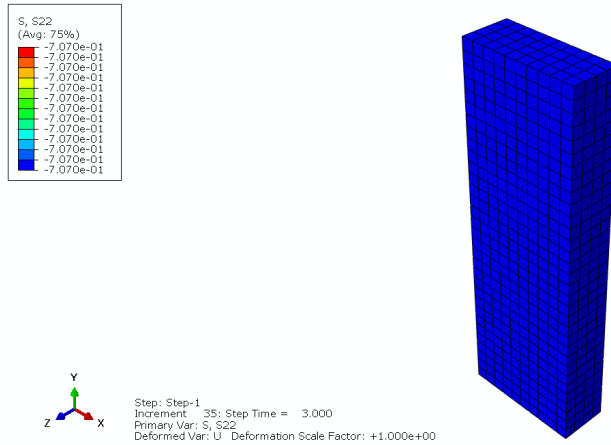


Figure 29 Stress S22 Results for AUB Wall (Main Longitudinal Axial – Uniform)

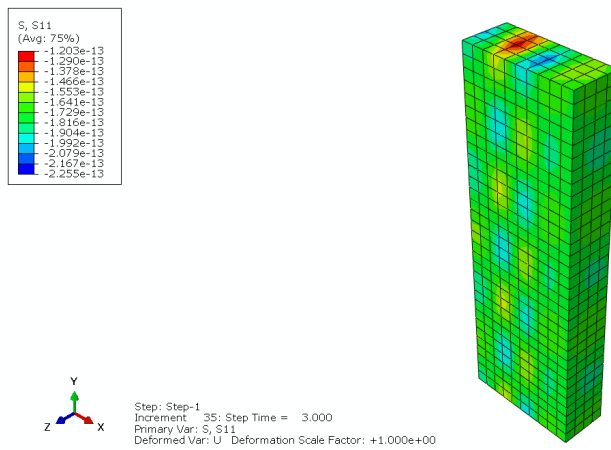


Figure 30 Stress S11 Results for AUB Wall (Secondary Lateral – Practically Zero)

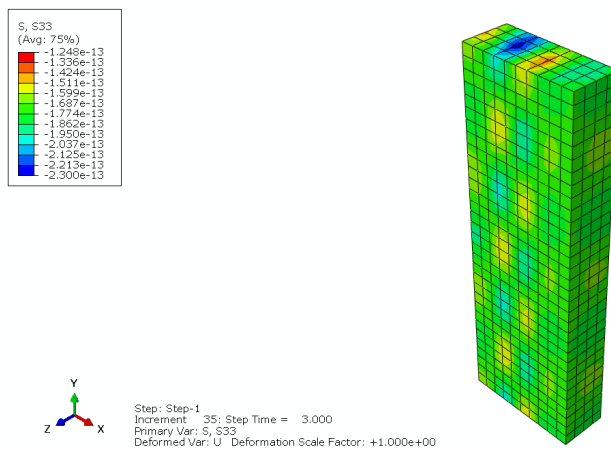


Figure 31 Stress S33 Results for AUB Wall (Secondary Out of Plane – Practically Zero)

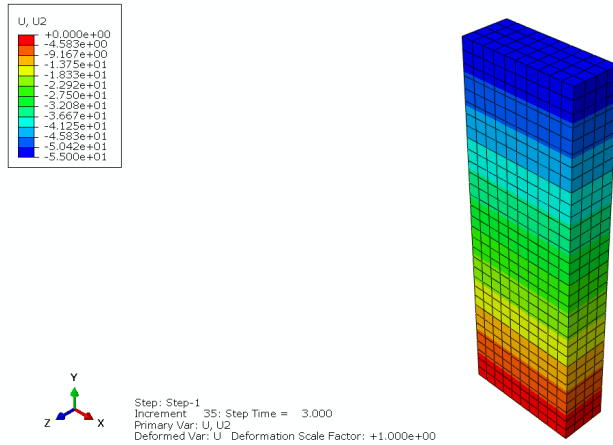


Figure 32 Displacement U2 Results for AUB Wall (Main Longitudinal Axial – Linear)

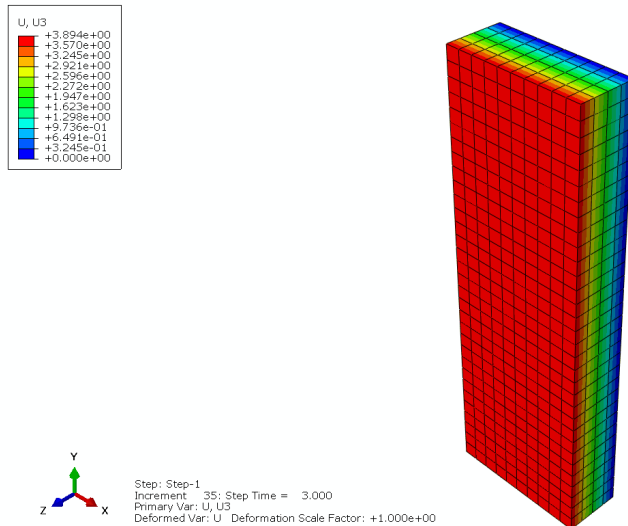


Figure 33 Displacement U3 Results for AUB Wall (Secondary Out of Plane – Linear)

The stress-strain curve obtained for the wall using CDP against the experimental one is shown in Figure 34.

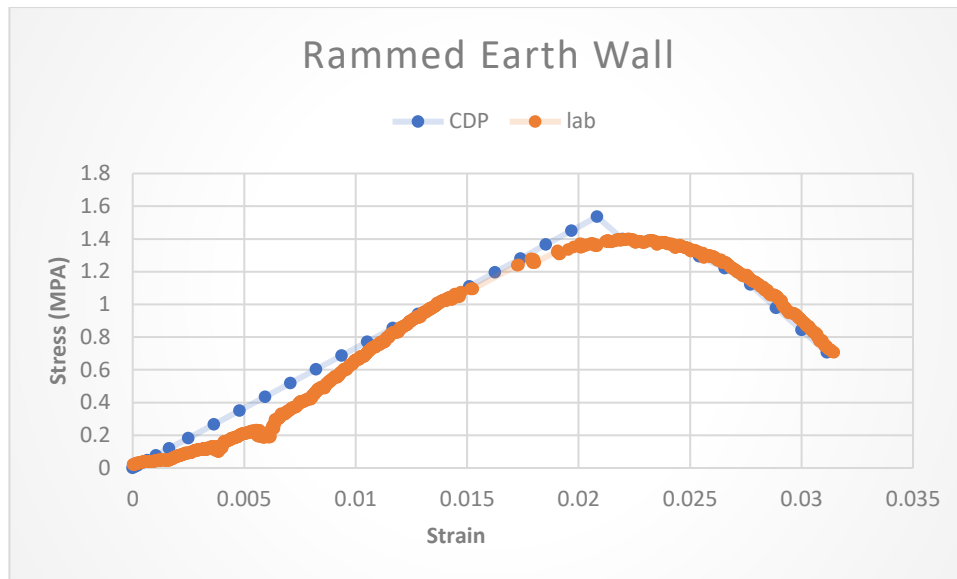


Figure 34 Stress-Strain Curve CDP and Experimental

The results show the uniform stress (or strain) distribution and linear displacement distribution along direction 2, as expected and obtained in the cylinders results earlier.

This section validates the use of ABAQUS on sample model walls with CDP nonlinear material for rammed earth.

4.2. Real size large wall of dimensions 5000 mm length, 2800 mm height, 400mm thickness with 600 mm x 600 mm square opening in the middle.

This wall shown in Figure 35, is the large-scale real wall that is modeled here in its full dimensions (5000 mm x 2800 mm x 400 mm), and includes a square opening of (600 mm x 600 mm) to show the type of results that will be obtained later for the quarter walls in full here.

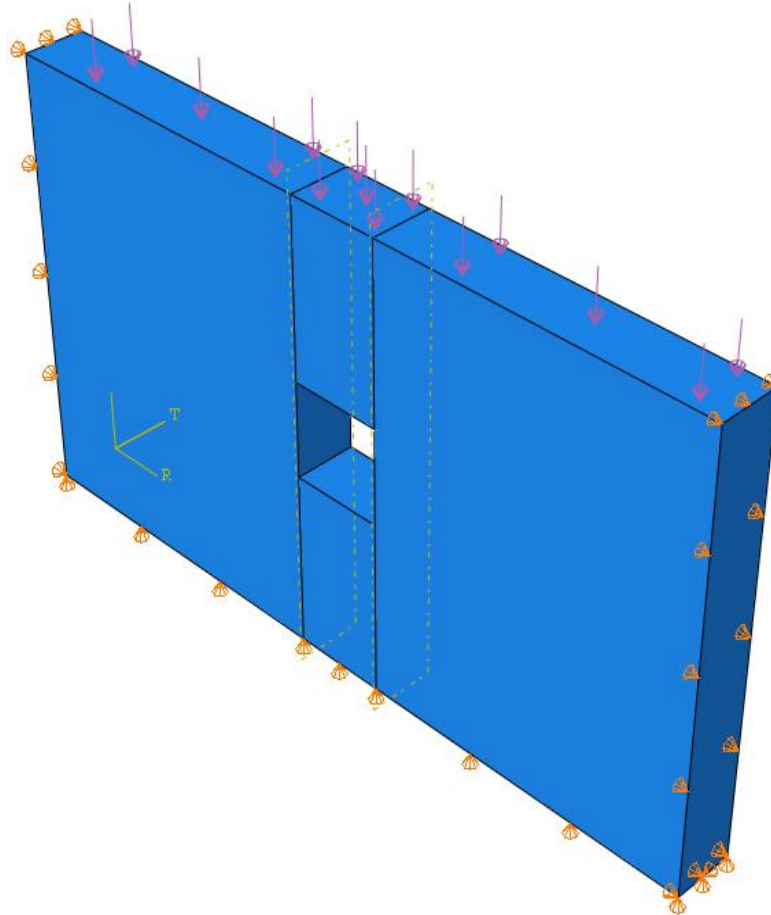


Figure 35 Full Real Wall (5000x2800x400) with (600x600) opening at the center

The wall has a density of 2.53 ton/mm³ and is constrained to move x direction. A pressure load of 0.05 N/mm³ was applied at the top. A mesh size of 200mm was used to minimize computation time (C3D8R Element type). The same stress-strain data used for the typical rammed earth cylinder from Ghazze were used here.

The results obtained are shown below in Figure 36 to Figure 41.

Note that directions 1 (or 11), 2 (or 22), 3 (or 33) indicate lateral along the width, longitudinal axial, and out-of-plane along the thickness, respectively.

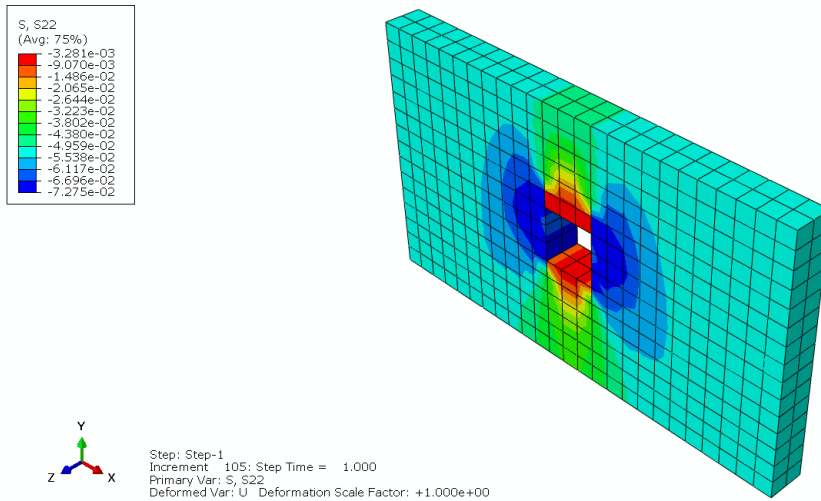


Figure 36 Stress S22 Results for the Wall (5000x2800x400) with (600x600) Opening at the Center (Main Longitudinal Axial – Uniform)

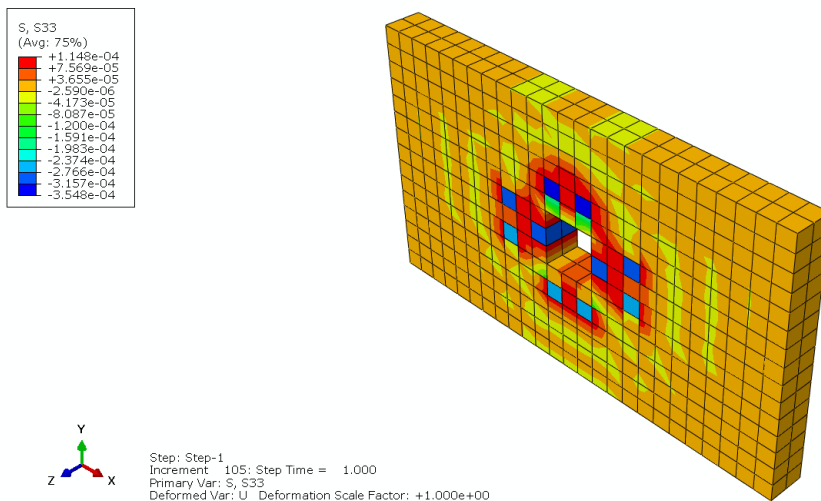


Figure 37 Stress S33 Results for the Wall (5000x2800x400) with (600x600) Opening at the Center (Secondary Out of Plane – Insignificant)

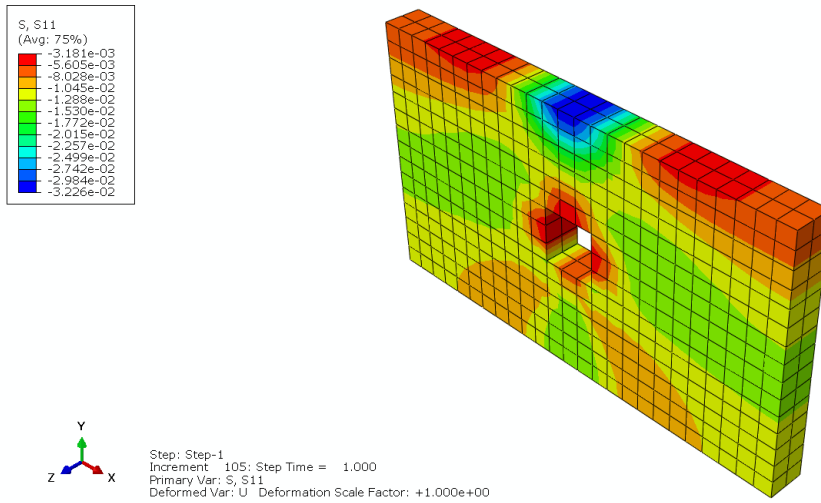


Figure 38 Stress S11 Results for the Wall (5000x2800x400) with (600x600) Opening at the Center (Secondary Radial)

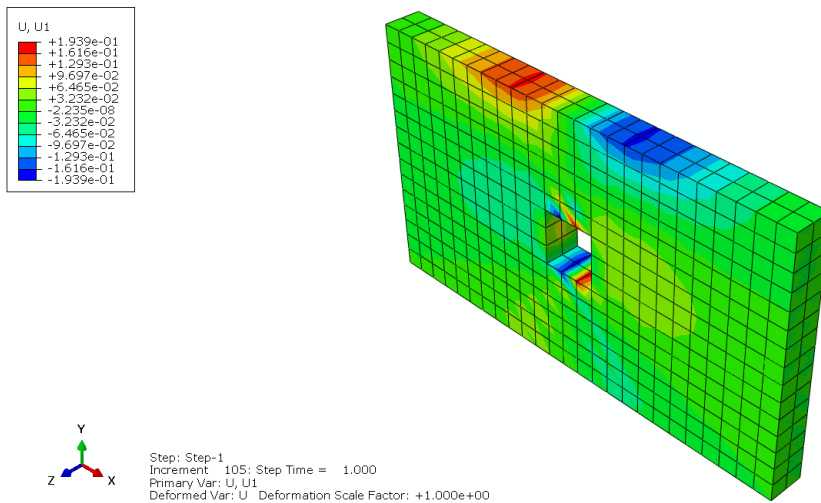


Figure 39 Displacement U1 Results for the Wall (5000x2800x400) with (600x600) Opening at the Center (Secondary Radial – Uniform)

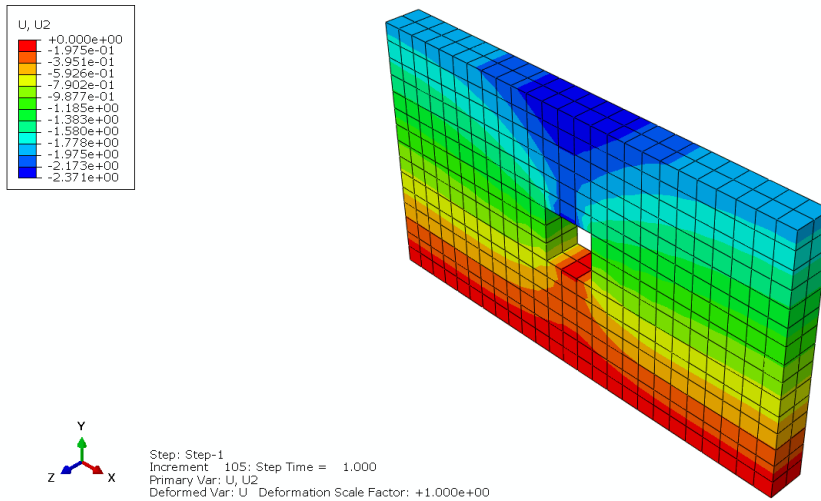


Figure 40 Displacement U2 Results for the Wall (5000x2800x400) with (600x600) Opening at the Center (Main Longitudinal Axial – Linear)

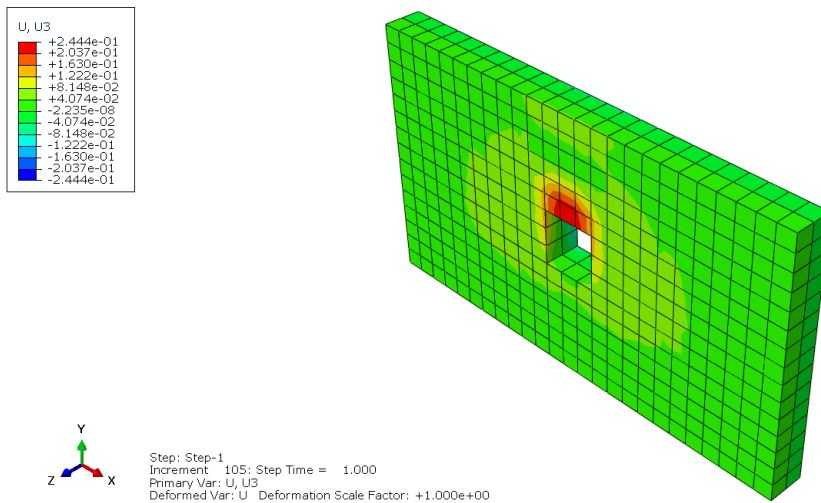


Figure 41 Displacement U3 Results for the Wall (5000x2800x400) with (600x600) Opening at the Center (Secondary Out of Plane – Uniform)

The Results show stress concentration around the opening with clear symmetric results along the y direction.

In the remainder of the models and due to bi-symmetry, and to minimize computation time, a quarter of the wall described in Section 4.2 was used for

continuing the modeling of rammed earth walls, with the boundaries as described in Section 4.1.

4.3. Validation for Quarter Rammed Earth Wall of Size 2500 mm wide, 2800 mm high and 200 mm thick, with no openings.

Figure 42 shows the quarter wall studied.

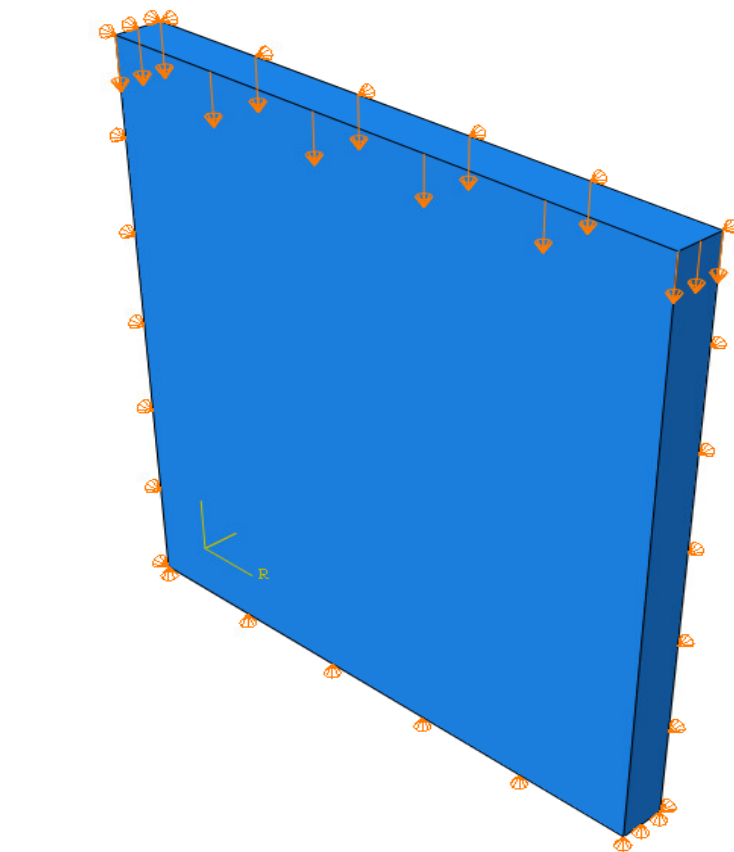


Figure 42 Quarter Rammed Earth Wall with No Opening.

The material properties and stress-strain data used for this wall were the same as inputted for the cylinder (mesh size 100, Element type C3D8R: An 8-node linear brick, reduced integration, hourglass control).

A displacement load of 120 mm was applied at the top with same boundary conditions used for the cylinder to existing AUB rammed earth wall (pinned at the left

bottom corner, restrained short and long vertical faces in x and z directions; and restrained at the bottom in the y direction).

The total force P induced by the 120 mm displacement loads was plotted against the displacement as shown in Figure 43.

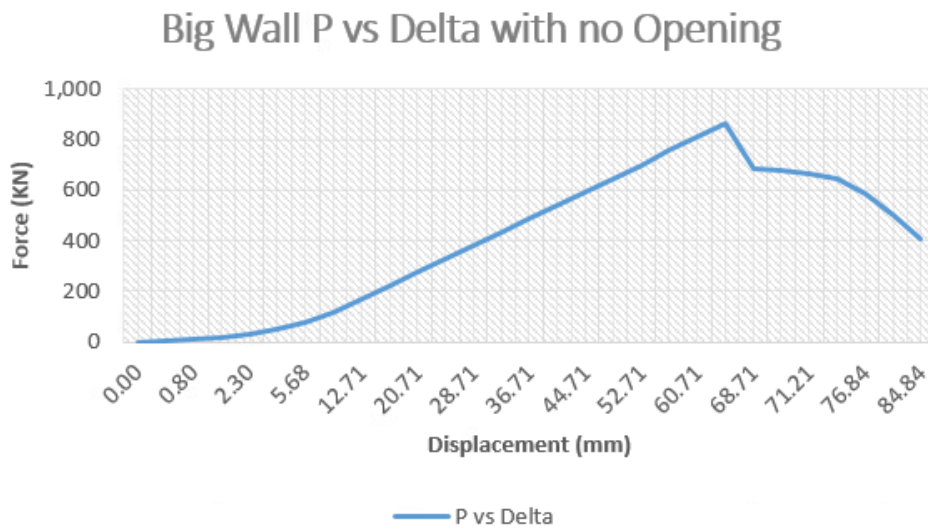


Figure 43 Load Displacement P-Delta for Large Wall

The axial stress S22 vs strain E22 curve is shown in Figure 44.

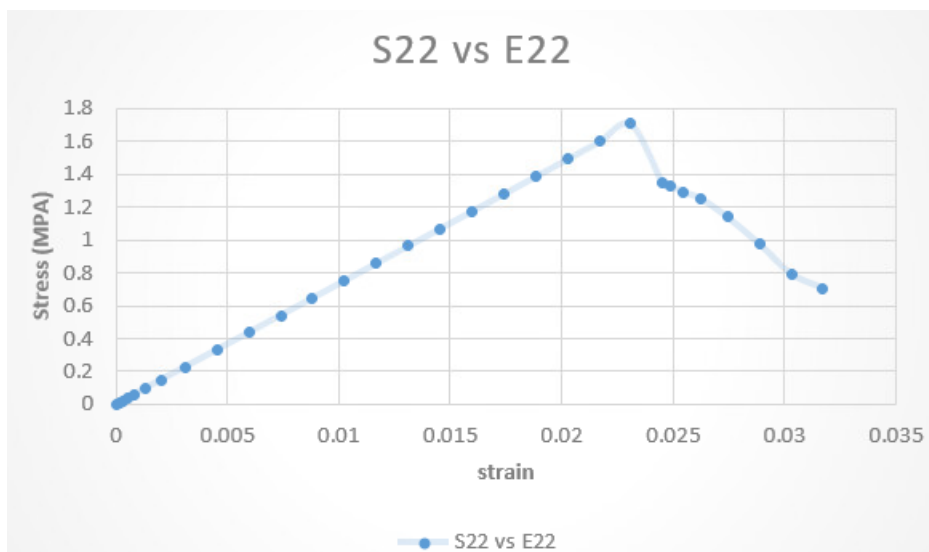


Figure 44 Stress-Strain S22 vs E22 Curve for Large Wall

The figures show close results to the stress-strain diagrams (and therefore load-displacement) of the existing AUB rammed earth wall.

After confirming that the wall model is working as required, the same wall dimensions and properties are considered, but with both short-width vertical faces constrained in the x direction, to represent a real wall boundary condition as part of a construction room.

Different models were analyzed and summarized below:

- A wall with no openings.
- A wall with square openings at the center:
 - Dimensions of 40 cm by 40 cm.
 - Dimensions of 60 cm by 60 cm.
 - Dimensions of 80 cm by 80 cm.
- A wall with circular openings at the center:
 - Diameter 40 cm.
 - Diameter 60 cm.
 - Diameter 80 cm.
- A model with a square opening of 60 cm by 60 cm located one-third from the top wall surface was considered.
- A model with a square opening of 60 cm by 60 cm located one-third from the bottom wall surface was considered.
- Stiff timber element with the same dimensions as the opening was also evaluated.

4.3.1. Case 1: Quarter Wall of Dimensions 2500m*2800m*200mm restrained along x direction on both short width vertical faces.

Figure 45 represents Case 1 Model

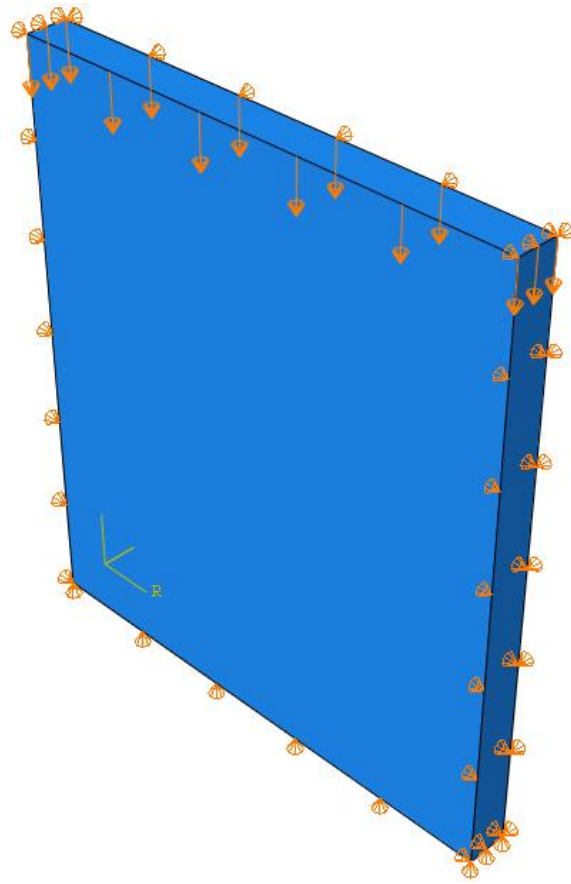


Figure 45 Case 1 Model

The mesh size used is 100 mm with C3D8R an 8-node linear brick, reduced integration, hourglass control type. The results for total load P applied due reaction forces and 80 mm displacement control are shown in Figure 46.

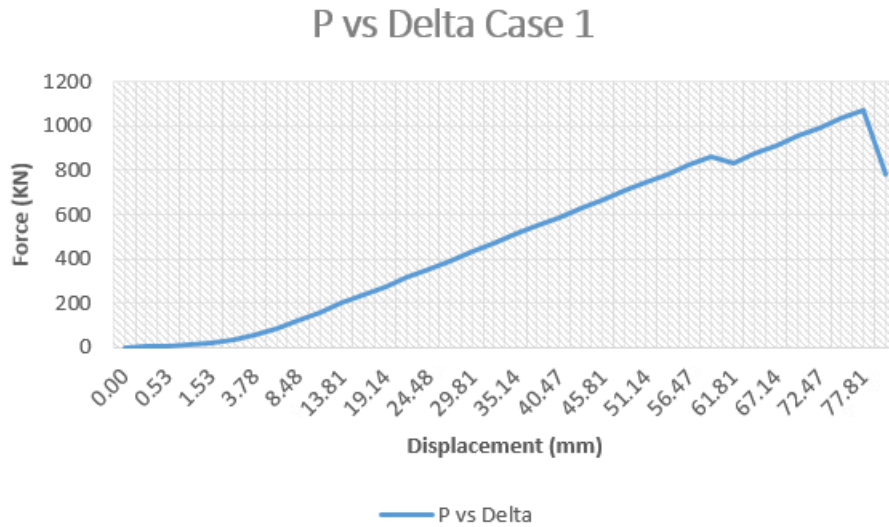


Figure 46 P-Delta Curve for Case 1

The axial stress S22 against the strain E22 curve obtained is shown in Figure 47.

The results are similar, but slightly different than the non-restrained wall, as expected.

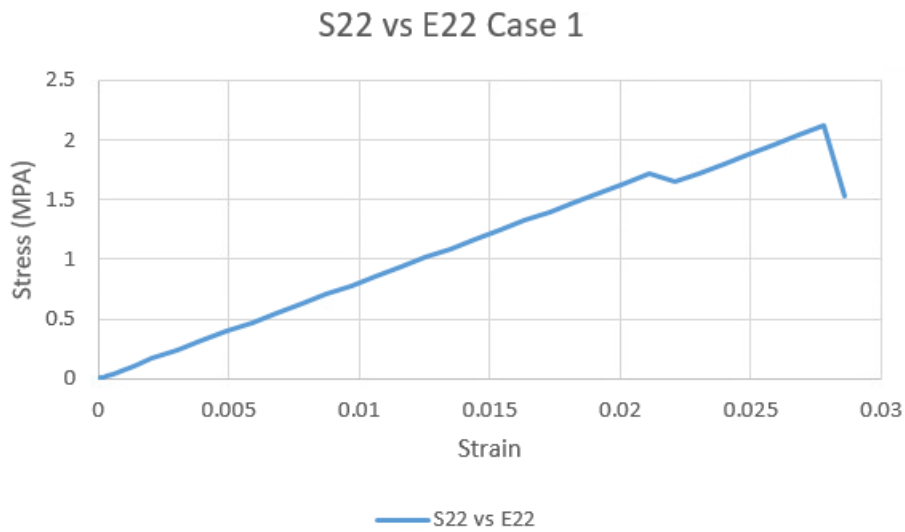


Figure 47 S22 vs E22 for Case 1

4.3.2. Case 2: Quarter Wall of Dimensions 2500m*2800m*200mm restrained along x direction on both short width vertical faces with 40cm by 40cm opening in the center.

Figure 48 shows Case 2.

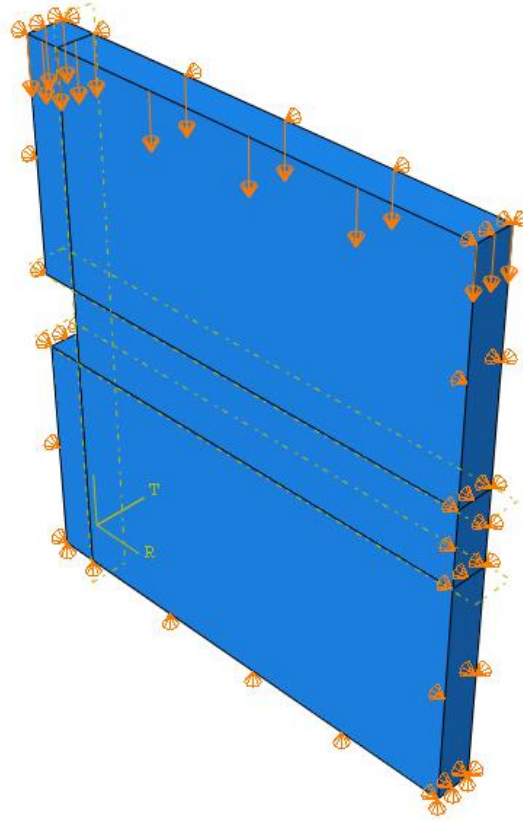


Figure 48 Case 2 Model

The mesh size used is 100 mm with C3D8R an 8-node linear brick, reduced integration, hourglass control type.

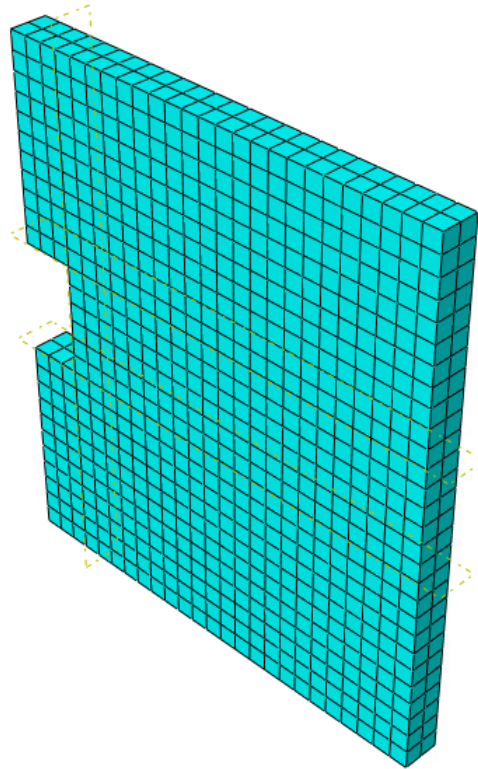


Figure 49 Mesh for Case 2

After adding the opening to the wall, nonlinearity appeared, and the mesh geometry required adjustments. To resolve that issue, partitions were used as shown in Figure 48 above. Additionally, the ABAQUS manual suggests using low viscosity values (around 0.001) in such cases to achieve faster convergence, though this may slightly affect the results.

The objective is summarized below:

- Plot the curve of the total force resulting from the vertical reaction forces against:
 - The displacement U2 at the top (center location).
 - U2 at the top of the opening (center location).
 - U2 at the bottom of the opening (center location).
- Plot the total force P against the stresses S11, S22, and S33 at each point.

The P – Delta curves for Case 2 are shown in Figure 50.

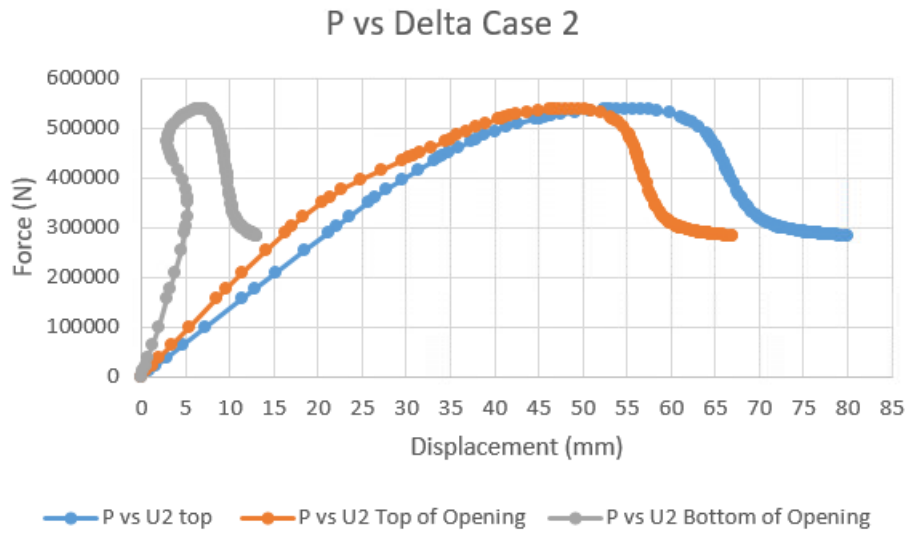


Figure 50 P-Delta Case 2

The force against stresses obtained for Case 2 are shown in Figure 51 and Figure 52.

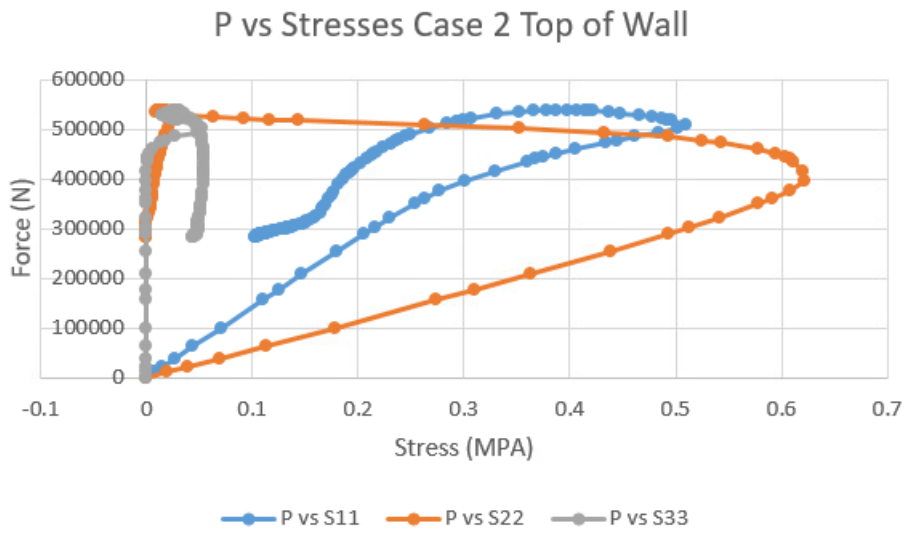


Figure 51 P vs S11, S22, S33 at Top of Wall for Case 2

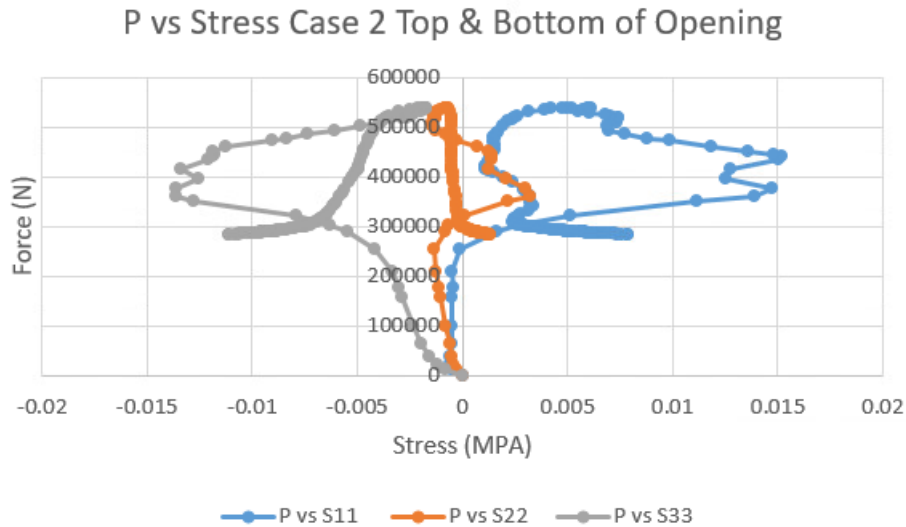


Figure 52 P vs S11, S22, S33 at Top and Bottom of Opening for Case 2

The above curves show that when going downwards in the opening, the force against displacement decreases. At the top of the wall, the force against S22 shows the largest effect, unlike at the boundaries of the opening. The difference in force against displacement at the top and bottom of the opening, despite having the same force against stress relationship, is primarily due to variations in stiffness and stress distribution around the opening. The stiffness near the top and bottom of the opening can differ due to factors like geometry, and boundary conditions, leading to different displacement responses under the same applied force.

While the stress distribution (S11, S22, S33) remains similar because it is governed by the overall force and material properties, the displacement varies because it is directly affected by the local stiffness.

Essentially, the same force can produce different displacements in regions with different stiffness, even if the stress at those points is similar. This explains the difference in force against displacement curves, compared to the force against stress curves, which do not differ.

At the top surface of the wall, the vertical stress component (S22) dominates because the wall primarily carries vertical loads. This results in a strong correlation between the applied force and S22. However, near the opening, the load path is disrupted, causing the vertical stress (S22) to decrease as the force is redistributed around the opening. In this region, the horizontal (S11) and out-of-plane (S33) stress components become more significant due to stress concentration effects around the edges of the opening.

As a result, the force against S22 becomes close to zero, while the force against S11 and force against S33 exhibit a larger effect due to the redistribution of stresses around the opening.

4.3.3. Case 3: Quarter Wall of Dimensions 2500m*2800m*200mm restrained along x direction on both short width vertical faces with 60cm by 60cm opening in the center.

The same setup, loading and boundary conditions were applied to the wall with larger opening size of 60 cm by 60 cm. The mesh size used is 100 mm with C3D8R an 8-node linear brick, reduced integration, hourglass control type, same as the one in Figure 49. The P-Delta curve for Case 3 is shown in Figure 53.

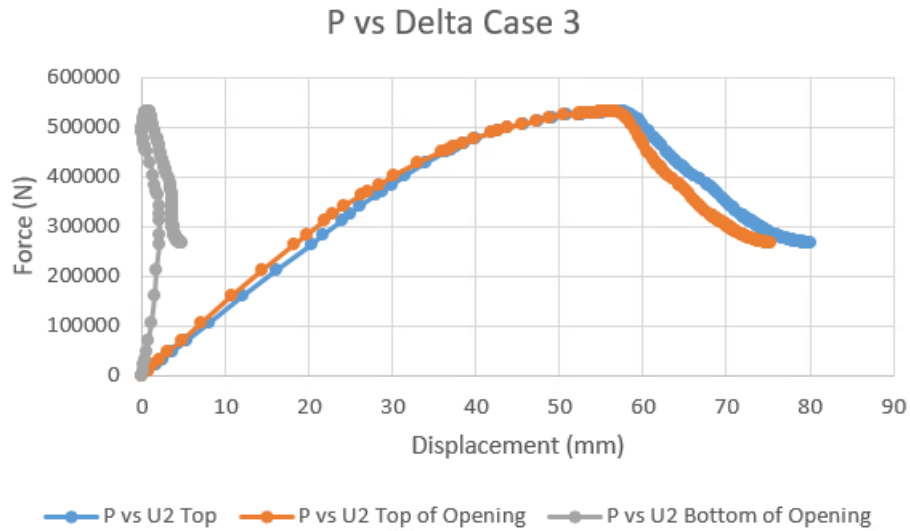


Figure 53 P-Delta for Case 3

As the size of the opening increases, the force against displacement at the top of the opening becomes closer to the force against displacement at the top of the wall. This occurs due to the increased uniformity in displacement, as discussed in previous sections. The force against displacement at the bottom of the opening become closer to zero.

The force against stresses obtained for case 3 are shown in Figure 54 and Figure 55.

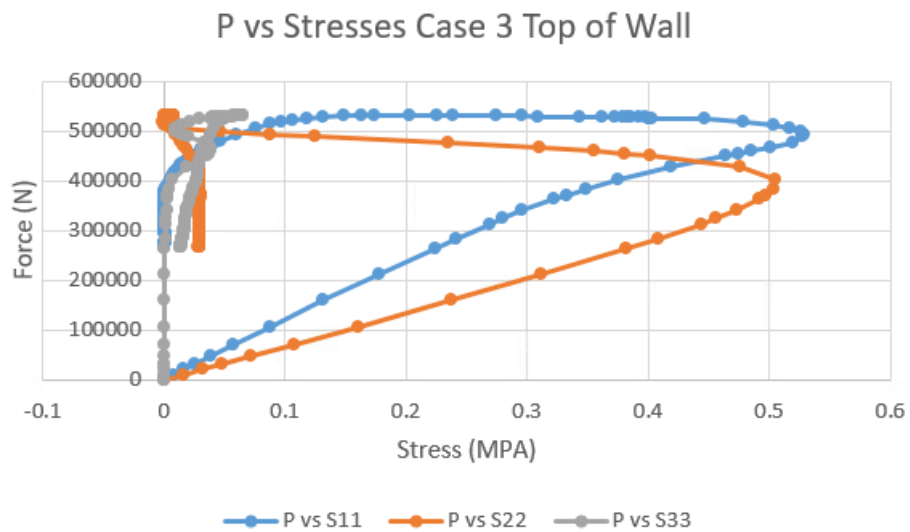


Figure 54 P vs S11, S22, S33 at Top of Wall for Case 3

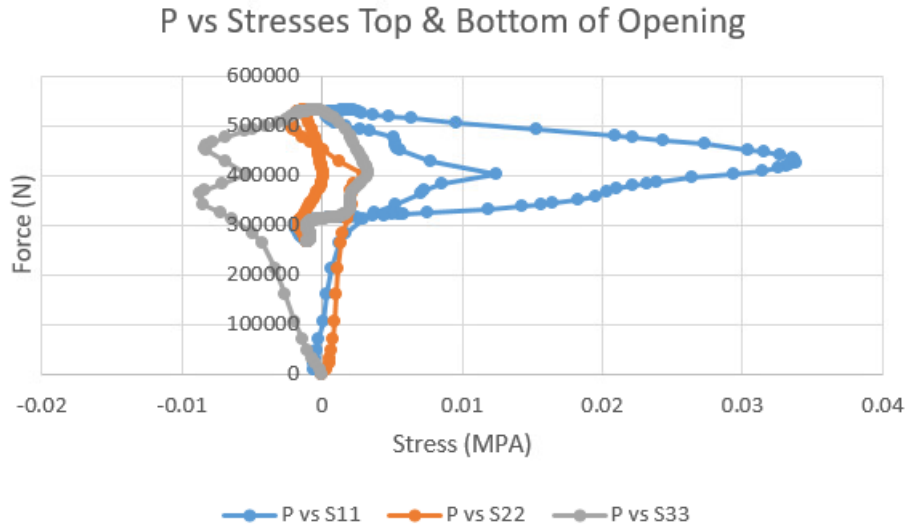


Figure 55 P vs S11,S22,S33 at Top and Bottom of Opening for Case 3

As the size of the opening increases from 40 cm by 40 cm to 60 cm by 60 cm, the stress distribution around the opening changes significantly. Larger openings disrupt the load path more, causing greater stress concentrations around the edges of the opening. This led to higher values of S11 and S33 (here mostly S11 due to applied boundary conditions) near the larger opening, while S22 shows a dramatic decrease.

4.3.4. Case 4: Quarter Wall of Dimensions 2500m*2800m*200mm restrained along x direction on both short width vertical faces with 80cm by 80cm opening in the center.

The same setup, loading and boundary conditions were applied to the wall with larger opening size of 80 cm by 80 cm. The mesh size used is 100 mm with C3D8R an 8-node linear brick, reduced integration, hourglass control type, same as the one in Figure 49. The P-Delta curve for Case 4 is shown in Figure 56.

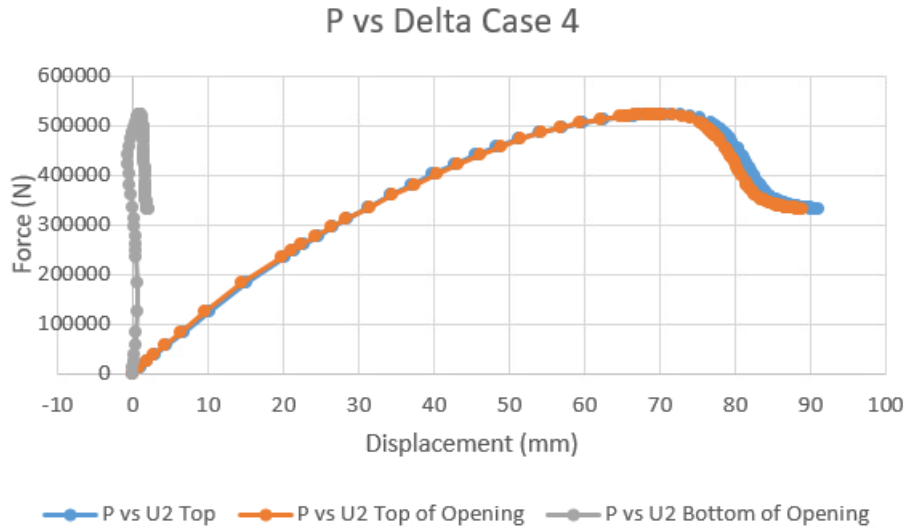


Figure 56 P-Delta for Case 4

The larger 80 cm by 80 cm opening led to a change in the wall's behavior, with higher displacement at failure and an altered force distribution. The area below the opening carried almost no load, while the wall above the opening bore most of the load.

The increased failure displacement for the larger opening suggests that the wall deforms more before failure, likely due to reduced stiffness and different stress distribution around the opening.

The force against stresses obtained for case 3 are shown in Figure 57 and Figure 58.

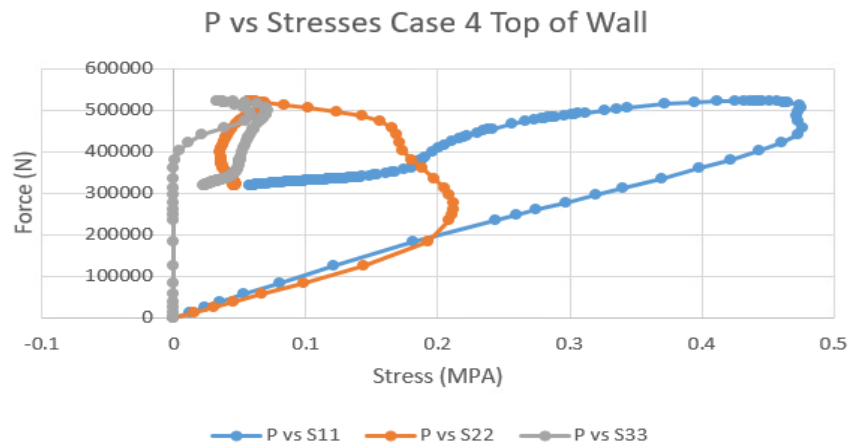


Figure 57 P vs S11, S22, S33 at Top of Wall for Case 4

As the size of opening increases, the total force against S11 increase and becomes dominant. This indicates that the stress distribution is significantly influenced by the opening size, causing higher stress concentrations along the direction of loading.

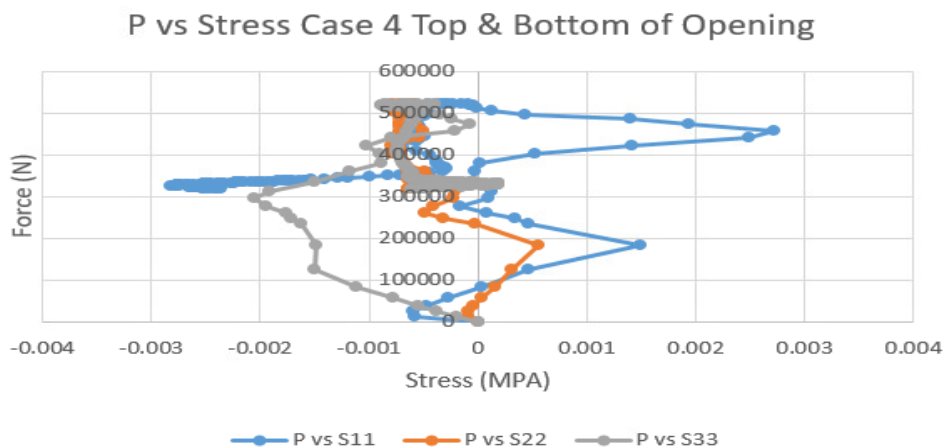


Figure 58 P vs S11, S22, S33 at Top and Bottom of Opening for Case 4

The above curve further indicates the dominance of stresses S11 and S22 as the opening size increases.

4.3.5. *Case 5: Quarter Wall of Dimensions 2500m*2800m*200mm restrained along x direction on both short width vertical faces with 60cm by 60cm opening located 1/3 from top (a), and 1/3 from bottom surface (b).*

4.3.5.1. Case Opening center 1/3 Apart from the Top Surface: Quarter Wall of Dimensions 2500m*2800m*200mm restrained along x direction on both short width vertical faces with 1 opening 60cm by 60cm located 1/3 from above surface.

Figure 59 below shows the case where a 60 cm by 60 cm opening is located one third from above surface. The load and boundary conditions remain the same.

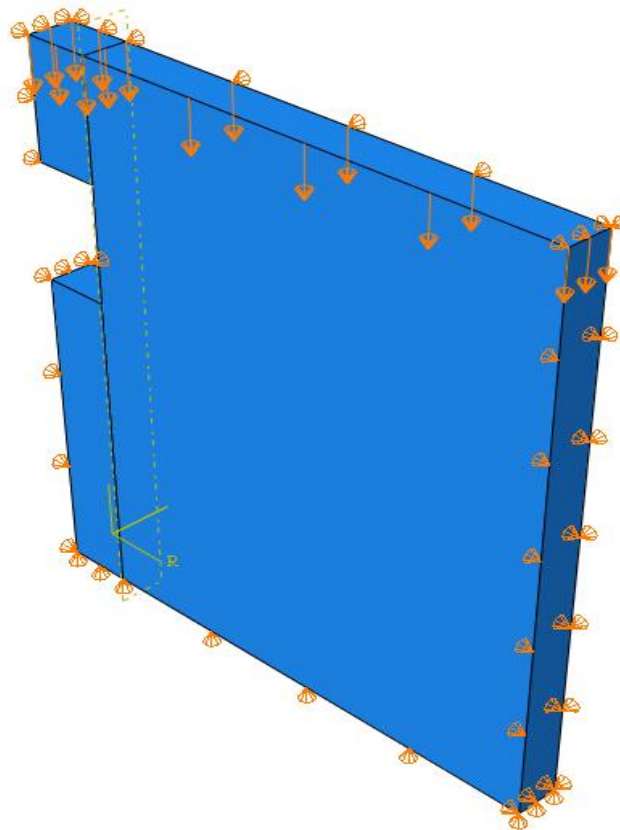


Figure 59 Wall with Opening on 1/3 Top Model

The mesh size used is 100 mm with C3D8R an 8-node linear brick, reduced integration, hourglass control type, and is shown in Figure 60.

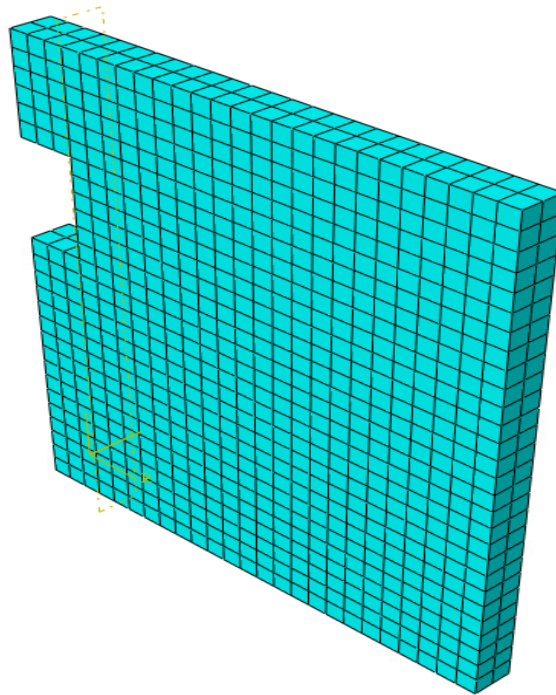


Figure 60 Mesh for Case 5 (a)

The P – Delta curves for Case 5 (a) are shown in Figure 61.

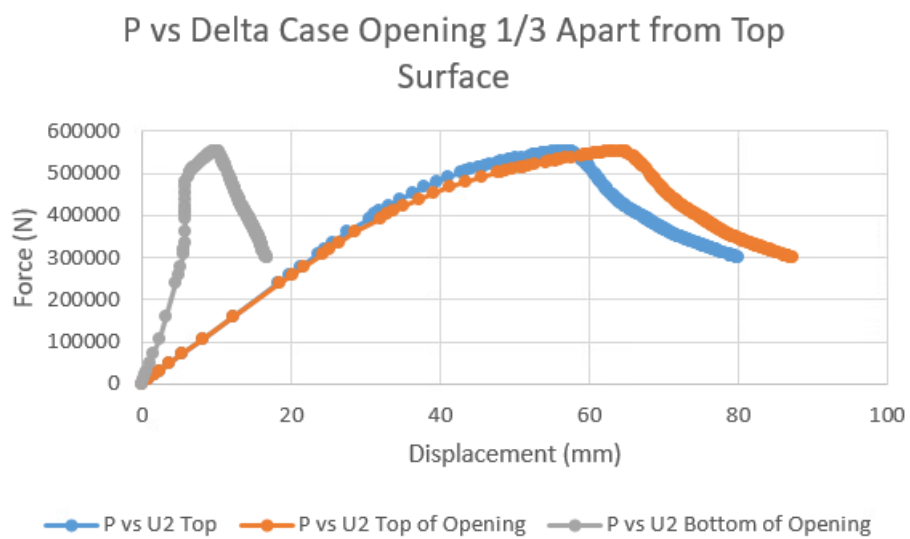


Figure 61 P-Delta for Case 5 (a)

As the opening is moved upward, the force-displacement curve at the top of the opening shifts to the right, crossing over the force-displacement curve at the top nodal surface. Meanwhile, the force-displacement ($P-\delta$) at the bottom of the opening remains low.

The force against stresses for Case 5 (a) are shown in Figure 62 to Figure 64.

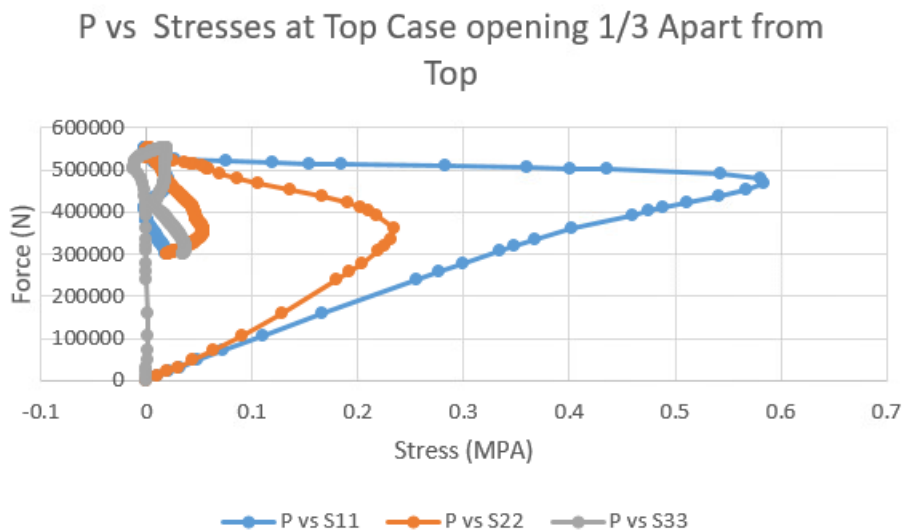


Figure 62 P vs S11, S22, S33 at Top of Wall for Case 5 (a)

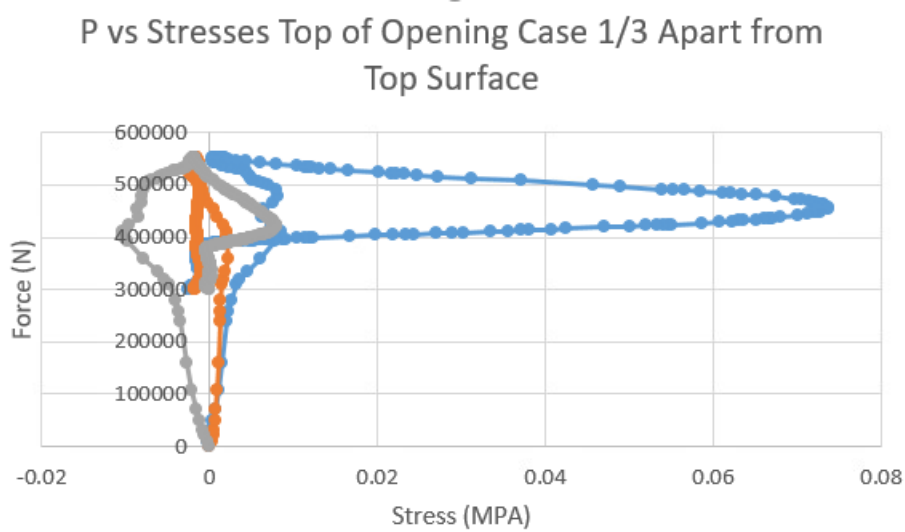


Figure 63 P vs S11, S22, S33 at Top of Opening for Case 5 (a)

P vs Stress at Bottom of Opening Case 1/3 Apart from Top

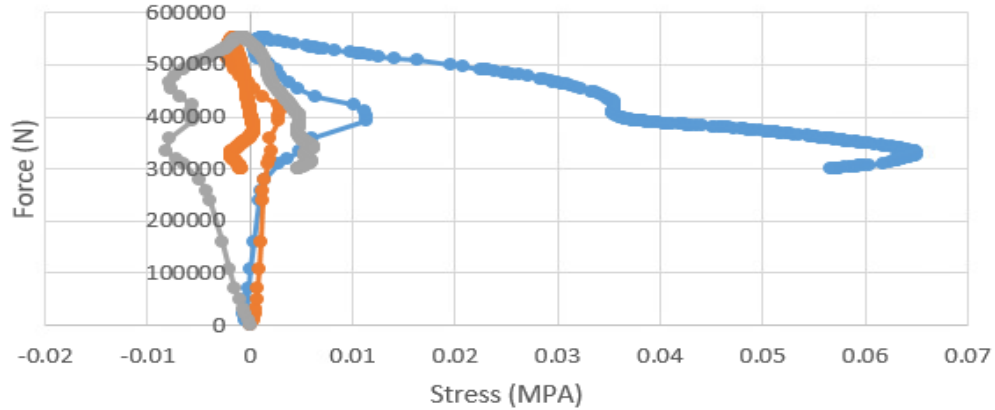


Figure 64 P vs S11, S22, S33 at Bottom of Opening for Case 5 (a)

This case demonstrates the dominance of transverse stresses. As the opening moves upward, the force versus vertical decreases.

4.3.5.2. Case Opening center 1/3 Apart from the Bottom Surface: Quarter Wall of Dimensions 2500m*2800m*200mm restrained along x direction on both short width vertical faces with 1 opening 60cm by 60cm located 1/3 from bottom surface.

Figure 65 below shows the case where a 60 cm by 60 cm opening is located one third from bottom surface. The load and boundary conditions remain the same.

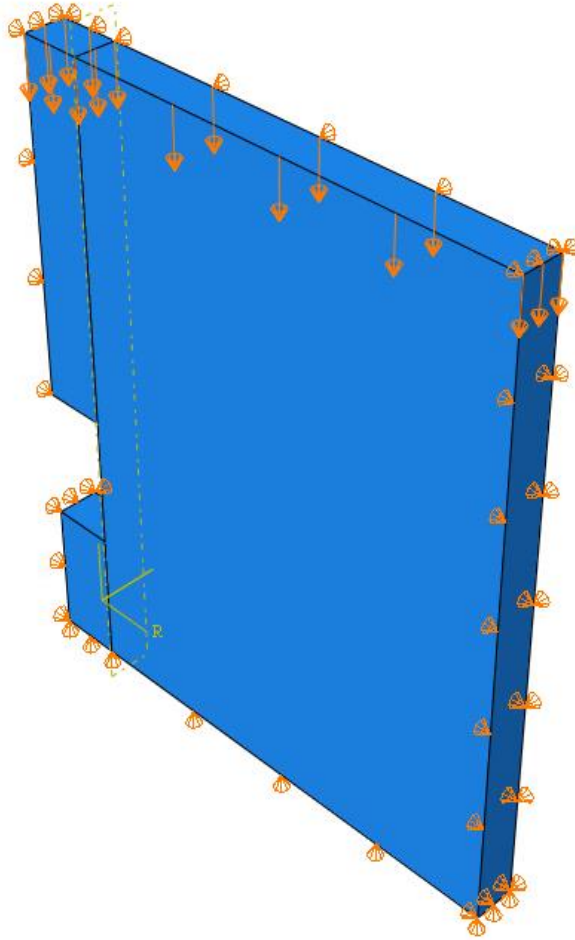


Figure 65 Wall with Opening on 1/3 Bottom Model

The mesh size used is 100 mm with C3D8R an 8-node linear brick, reduced integration, hourglass control type, and is shown in Figure 66.

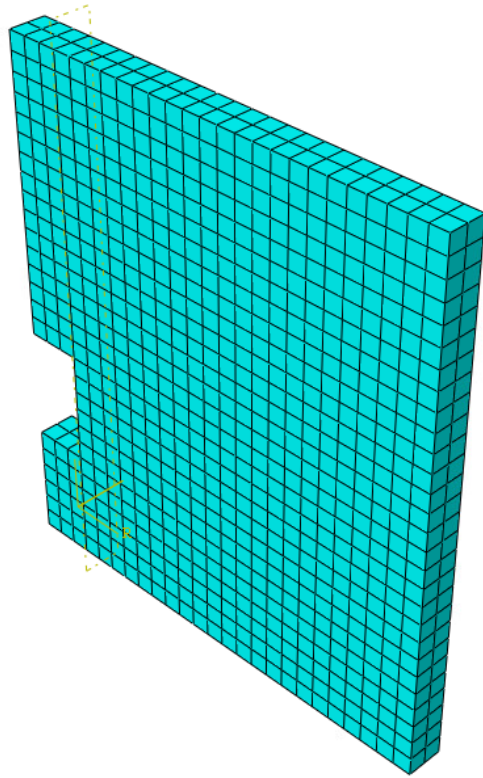


Figure 66 Mesh for Case 5 b

The P – Delta curves for Case 5 (b) are shown in Figure 67.

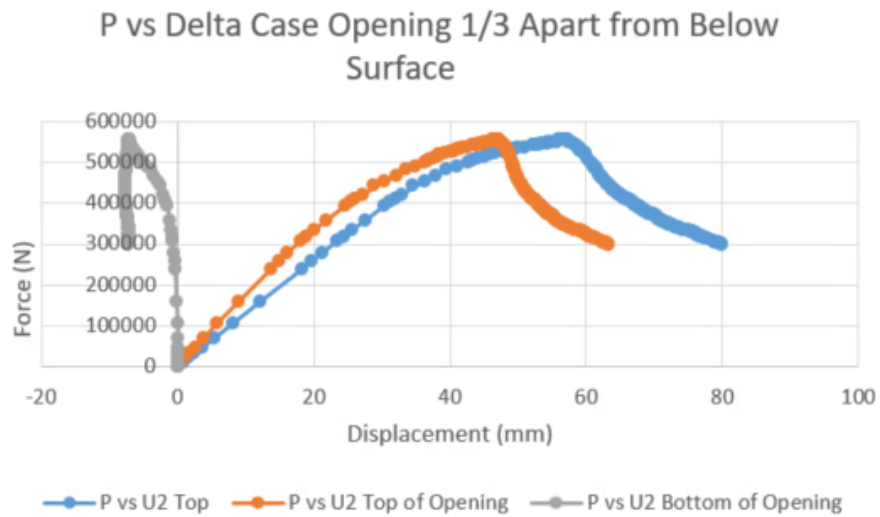


Figure 67 P-Delta for Case 5 (b)

As the opening is moved downward from the center, the force-displacement curve at the top of the opening shifts to the left, crossing over the force-displacement

curve at the top nodal surface. Meanwhile, the force-displacement ($P-\delta$) at the bottom of the opening becomes negative.

The force against stresses for Case 5 (a) are shown in Figure 68 to Figure 70.

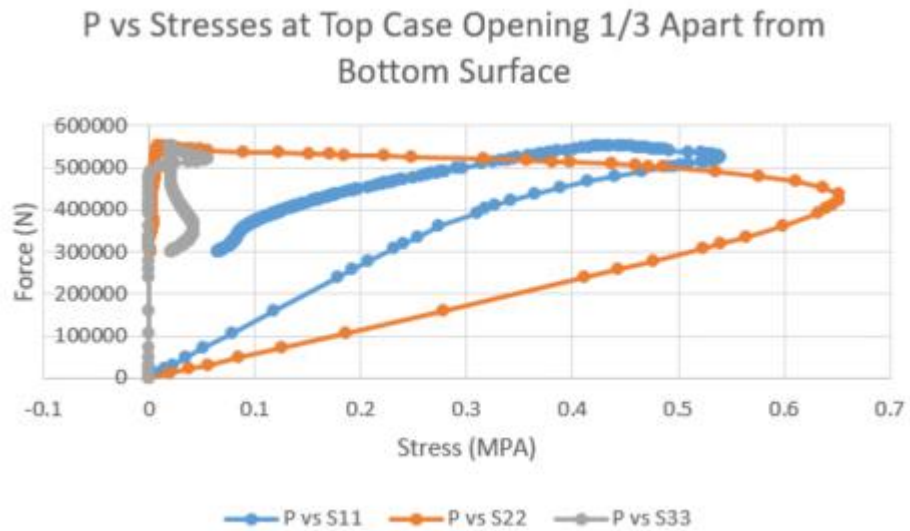


Figure 68 P vs S11, S22, S33 at Top of Wall for Case 5 (b)

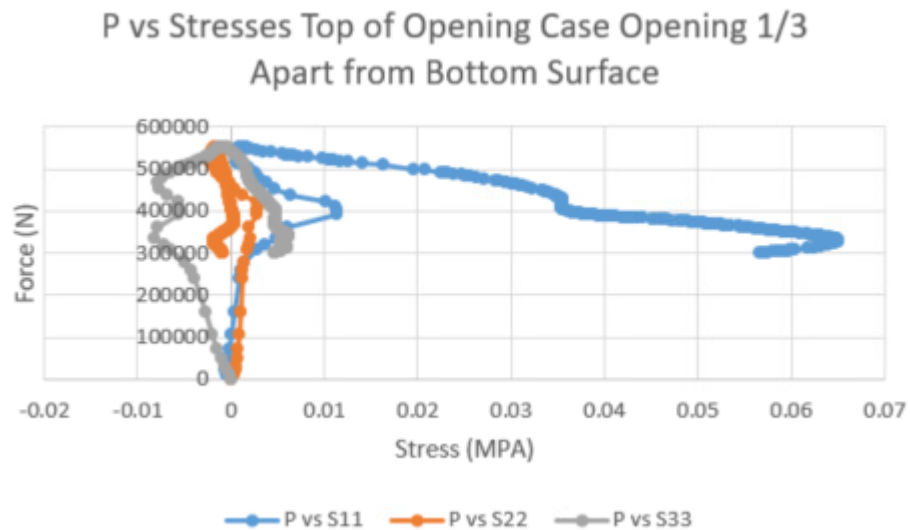


Figure 69 P vs S11, S22, S33 at Top of Opening for Case 5 (b)

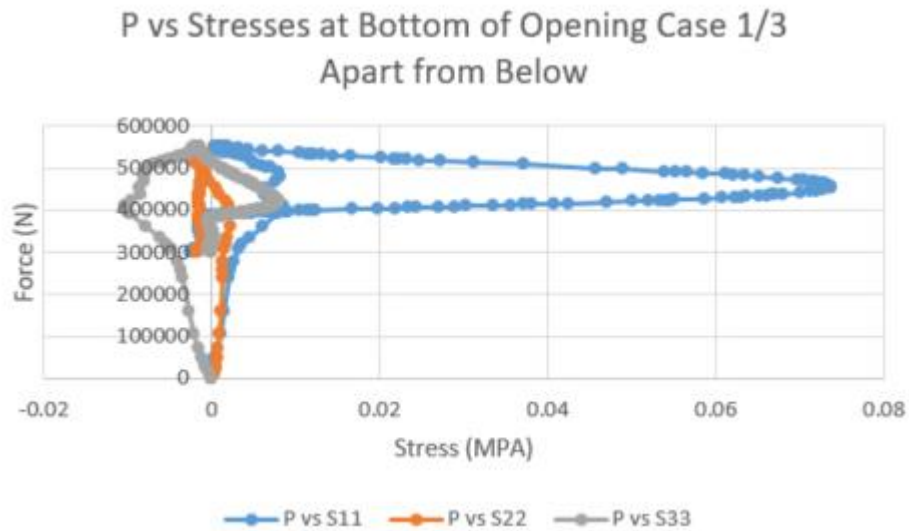


Figure 70 P vs S11,S22,S33 at Bottom of Opening for Case 5 (b)

As the opening moves below the center, the force versus displacement at the top nodal surface becomes more significant. At the nodes around the opening, the transverse stresses are more prominent.

4.3.6. Case 6: Quarter Wall of Dimensions 2500m*2800m*200mm restrained along x direction on both short width vertical faces with circular opening of 40cm diameter in the center.

Figure 71 shows Case 6 where a circular opening in the center of the wall is made. The boundary conditions remain the same as before.

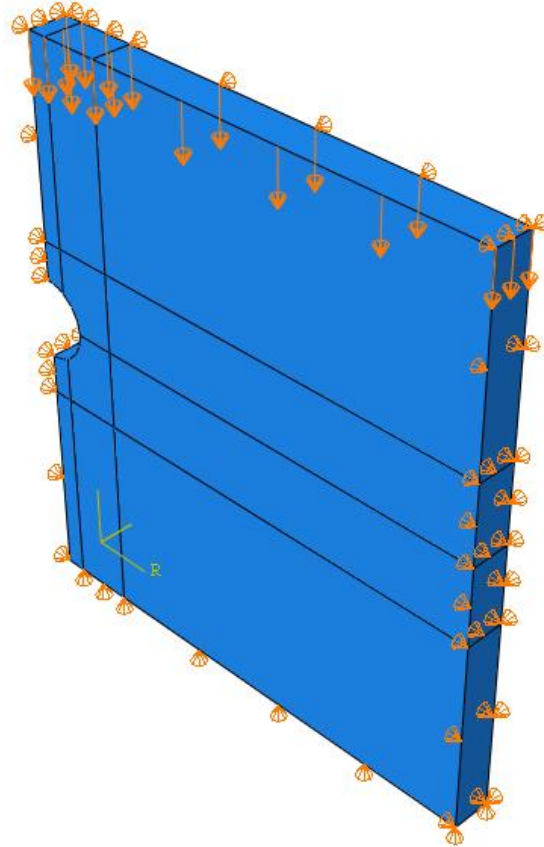


Figure 71 Wall with Circular Opening Case 6

The mesh size used is 100 mm with C3D8R an 8-node linear brick, reduced integration, hourglass control type, and is shown in Figure 72.

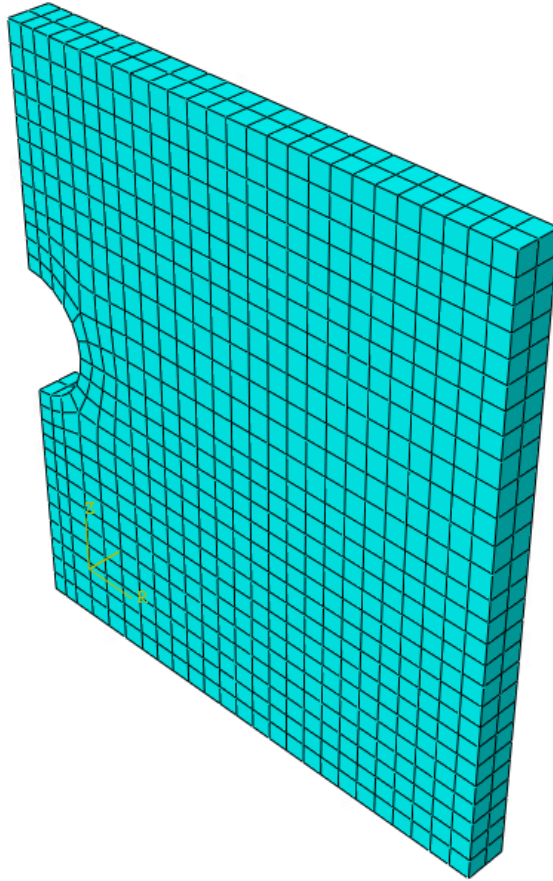


Figure 72 Mesh for Case 6

The P – Delta curve obtained for Case 6 is shown in Figure 73.

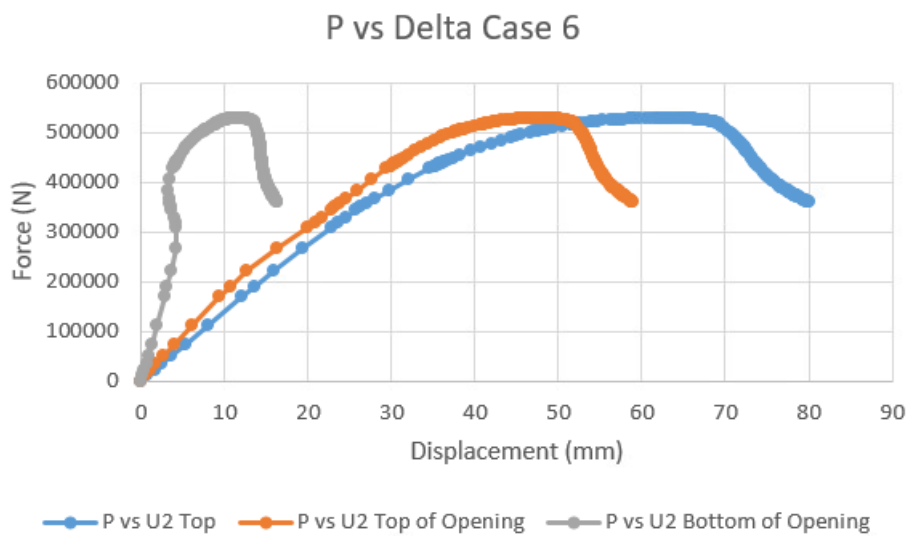


Figure 73 P-Delta for Case 6

The force against displacement in case of 40 cm diameter circular opening shows almost the same result as that for 40 cm by 40 cm square opening. However, the wall with circular opening showed almost better stability at the top surface node where it failed at around 70 mm displacement compared to the wall with square opening that failed at around 60 mm.

The force against stresses for Case 6 are shown in Figure 74 to Figure 76.

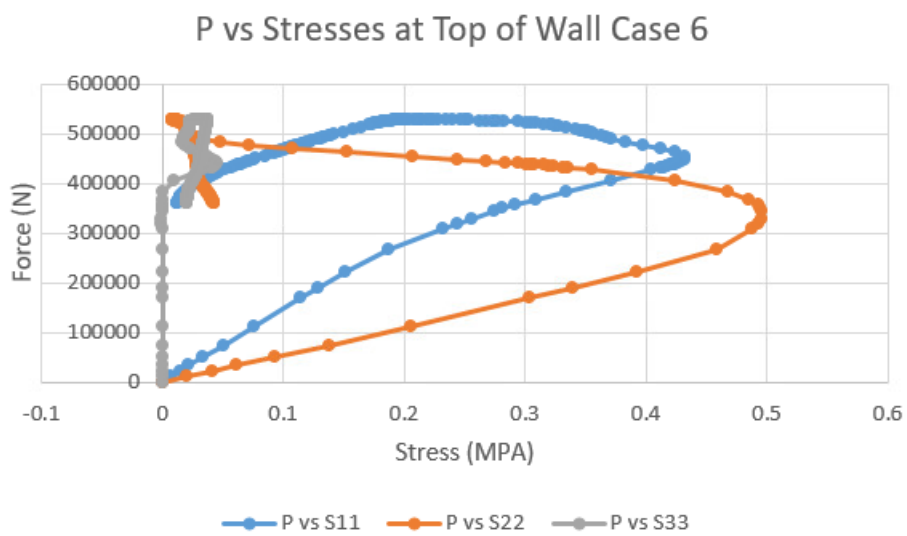


Figure 74 P vs S11,S22,S33 at Top of Wall for Case 6

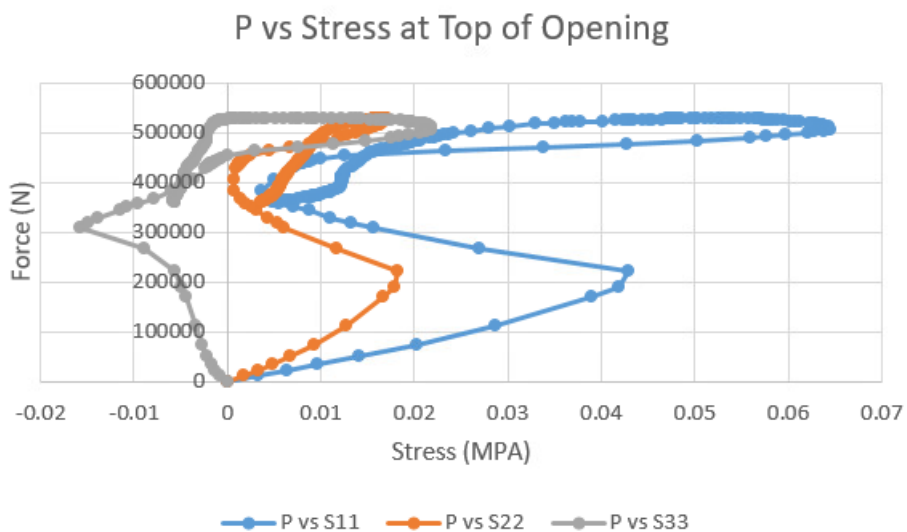


Figure 75 P vs S11, S22, S33 at Top of Opening for Case 6

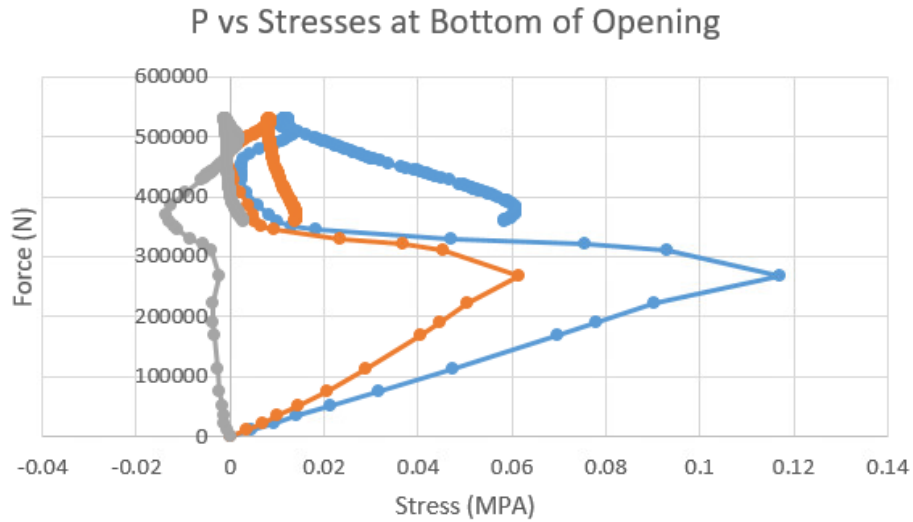


Figure 76 P vs S11, S22, S33 at Bottom of Opening for Case 6

The square opening's geometry leads to a more consistent stress distribution at the top and bottom, whereas the circular opening's curved shape causes a difference in stress distribution, resulting in the observed differences in force against stress behavior.

4.3.7. Case 7: Quarter Wall of Dimensions 2500m*2800m*200mm restrained along x direction on both short width vertical faces with circular opening of 60cm diameter in the center.

The mesh size used is 100 mm with C3D8R an 8-node linear brick, reduced integration, hourglass control type, same as the one in Figure 72.

The P – Delta curve obtained for Case 7 is shown in Figure 77.

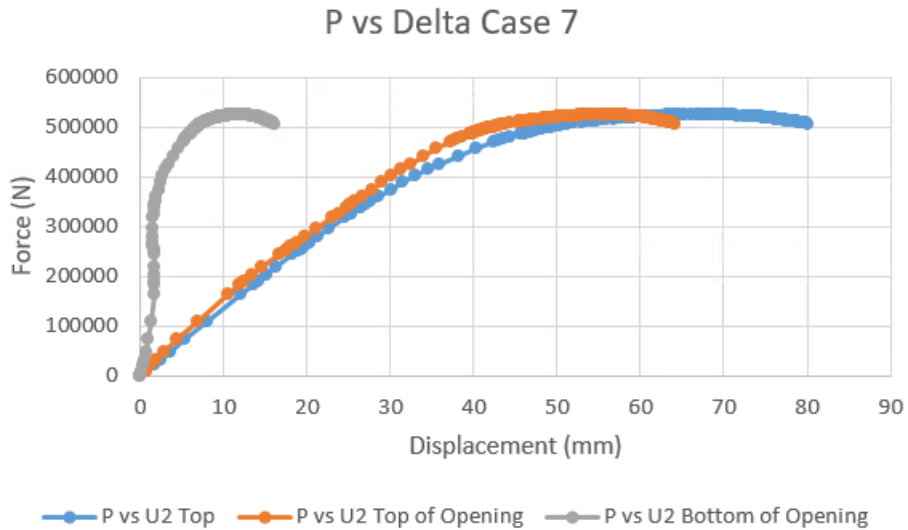


Figure 77 P-Delta for Case 7

The curve above shows that when increasing the diameter of the opening the failure is shifted and the force against displacement at the top of the opening is starting to converge with that at the top surface of the wall.

The force against stresses for Case 7 are shown in Figure 78 to Figure 80.

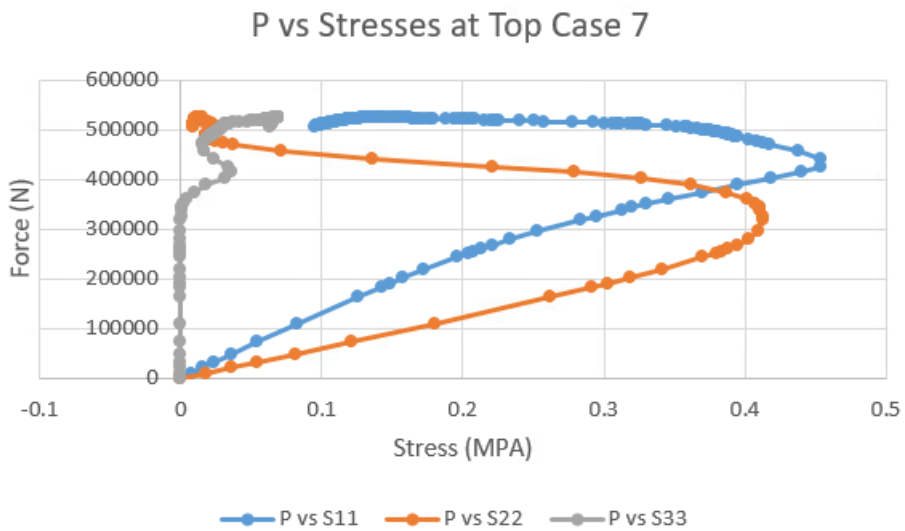


Figure 78 P vs S11,S22,S33 at Top of Wall for Case 7

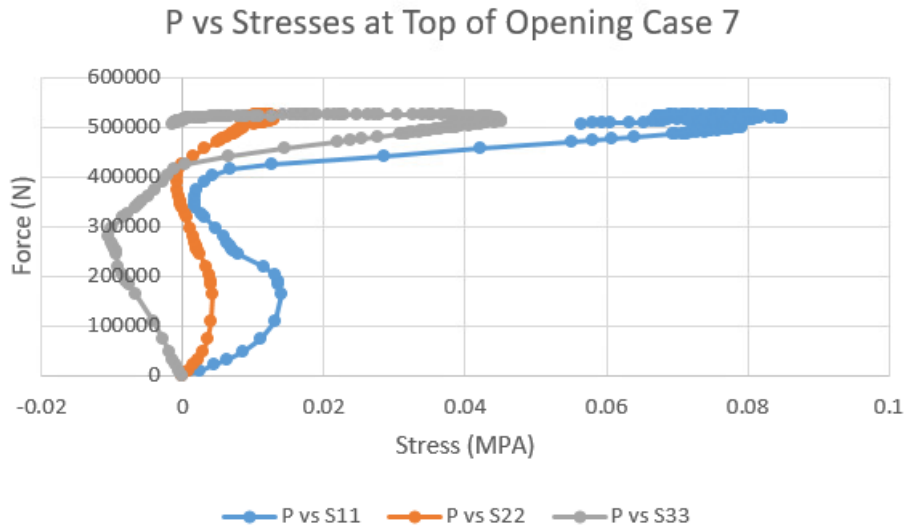


Figure 79 P vs S11,S22,S33 at Top of Opening for Case 7

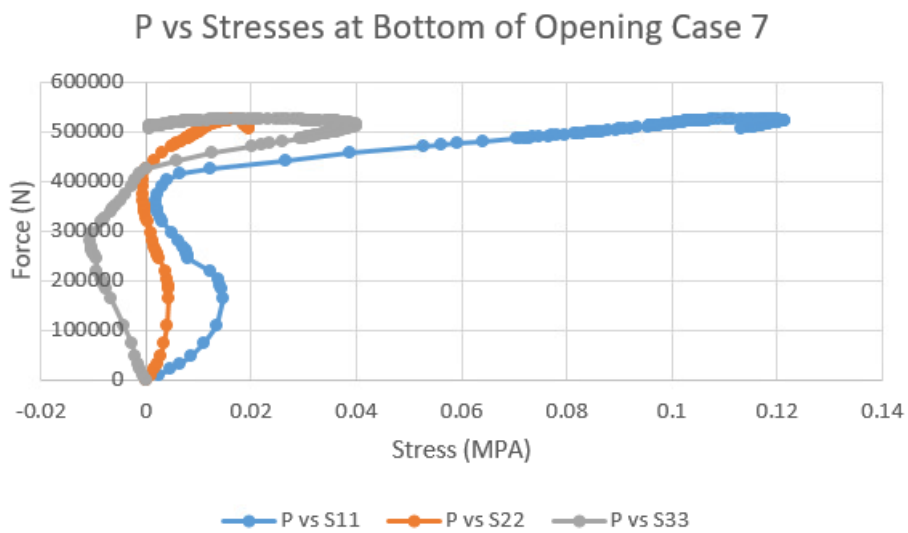


Figure 80 P vs S11,S22,S33 at Bottom of Opening for Case 7

The force against stresses is mainly dominated by the out of plane stresses. In this case, the force against stresses curves at the top and bottom of opening are different.

4.3.8. Case 8: Quarter Wall of Dimensions 2500m*2800m*200mm restrained along x direction on both short width vertical faces with circular opening of 80cm diameter in the center.

The mesh size used is 100 mm with C3D8R an 8-node linear brick, reduced integration, hourglass control type, same as the one in Figure 72.

The P – Delta curve obtained for Case 7 is shown in Figure 81.

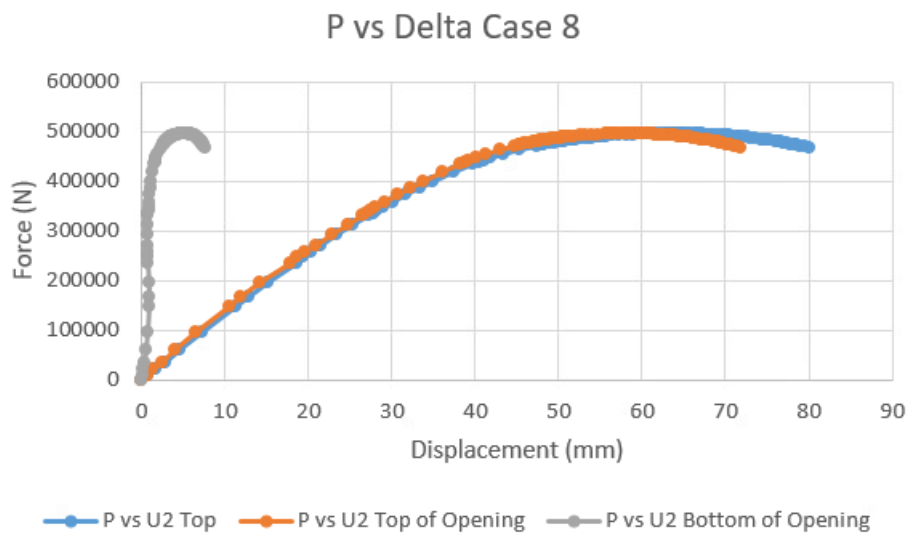


Figure 81 P-Delta for Case 8

The force against stresses for Case 8 are shown in Figure 82 to Figure 84.

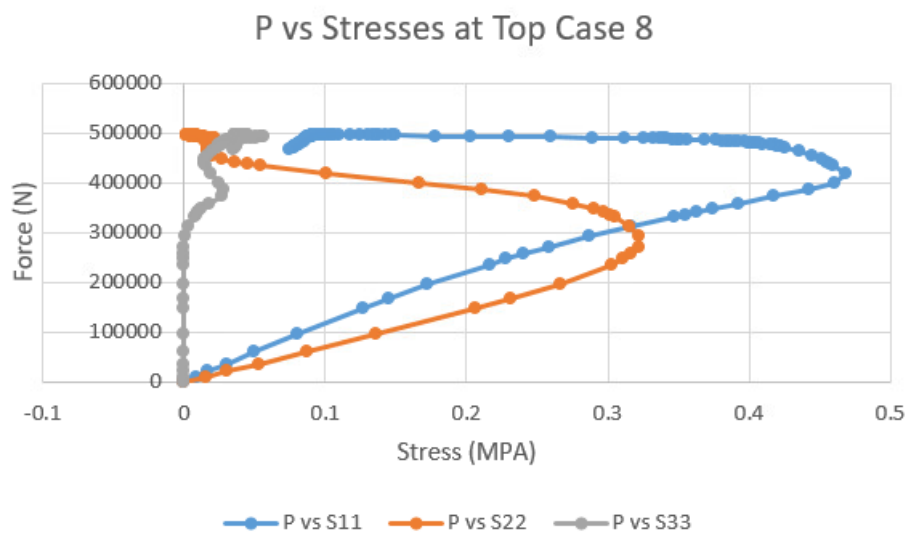


Figure 82 P vs S11, S22, S33 at Top of the Wall for Case 8

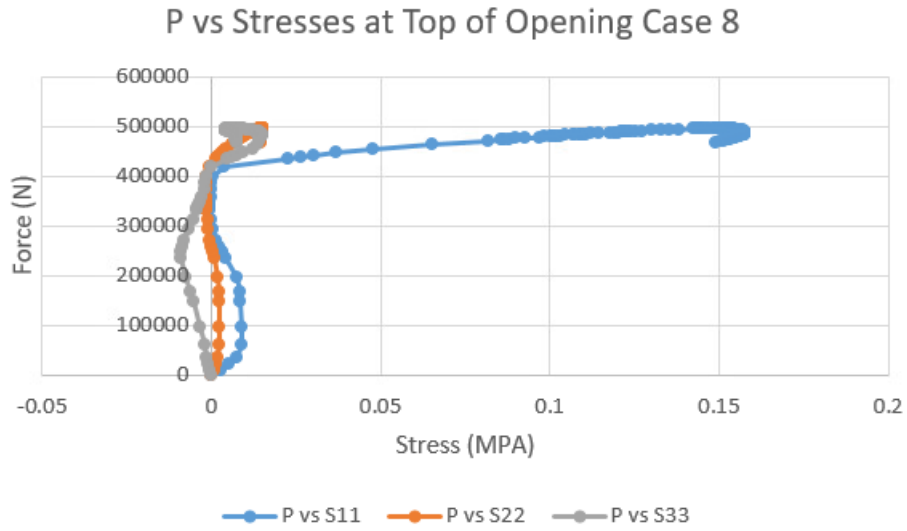


Figure 83 P vs S11, S22, S33 at Top of the Opening for Case 8

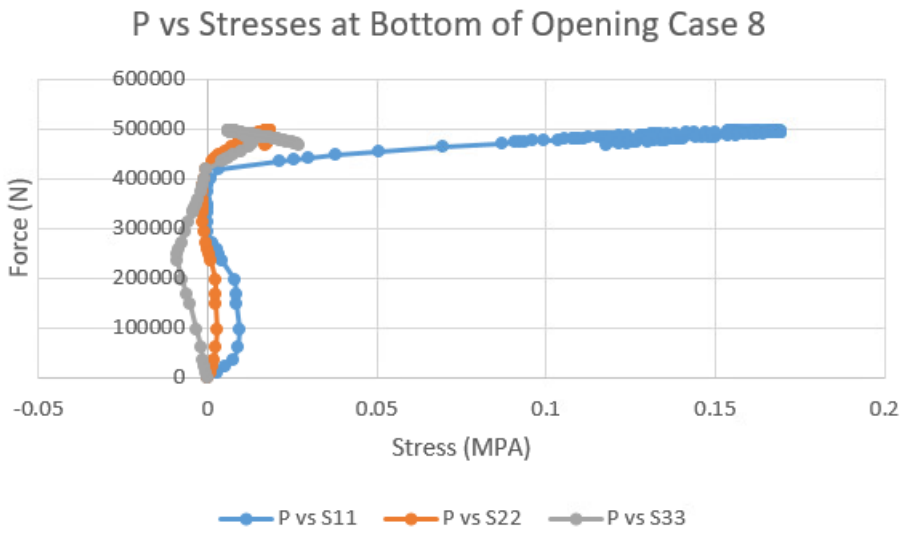


Figure 84 P vs S11, S22, S33 at Bottom of the Opening for Case 8

The results obtained are similar to the model with 60 cm diameter circular opening.

4.3.9. Cases 9-10: Quarter Wall of Dimensions 2500m*2800m*200mm restrained along x direction on both short width vertical faces with square opening of 60 cm by 60 cm (Case 9) and circular opening 60 cm diameter (Case 10) square with stiffened teak wood of $E=20\text{GPa}$.

Considering the case of the wall with 60 cm square opening. A teak wood 10 mm thick stiffener of modulus of elasticity 20 GPa is tied to the opening. Similar approaches as before to calculate force against displacements and force against stresses were considered here. The mesh size used is 100 mm with C3D8R an 8-node linear brick, reduced integration, hourglass control type.

The P – Delta curves obtained for Case 9 and Case 10 are shown in Figure 85 and Figure 86.

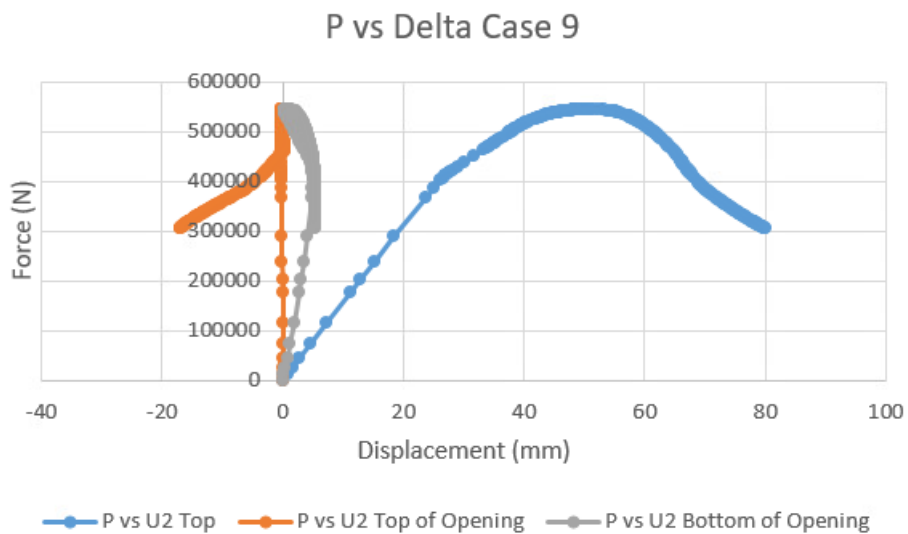


Figure 85 P-Delta for Case 9

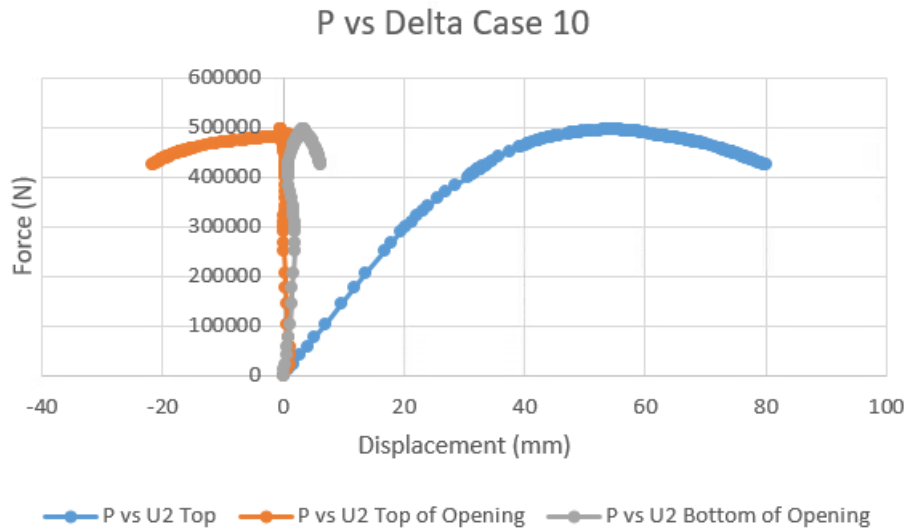


Figure 86 P-Delta for Case 10

The displacement at the opening is almost negligible compared to the top surface displacement.

The force against stresses for Case 9 and 10 are shown in Figure 87 to Figure 92.

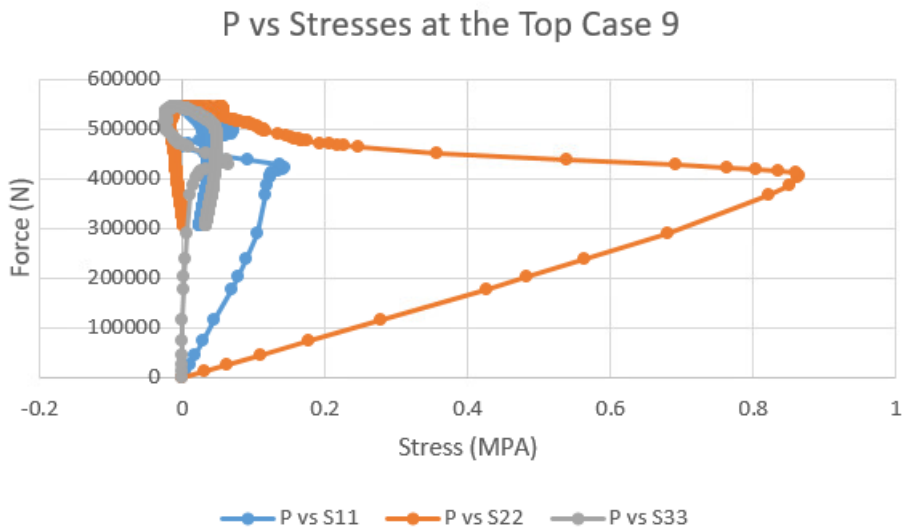


Figure 87 P vs S11, S22, S33 at Bottom of Wall for Case 9

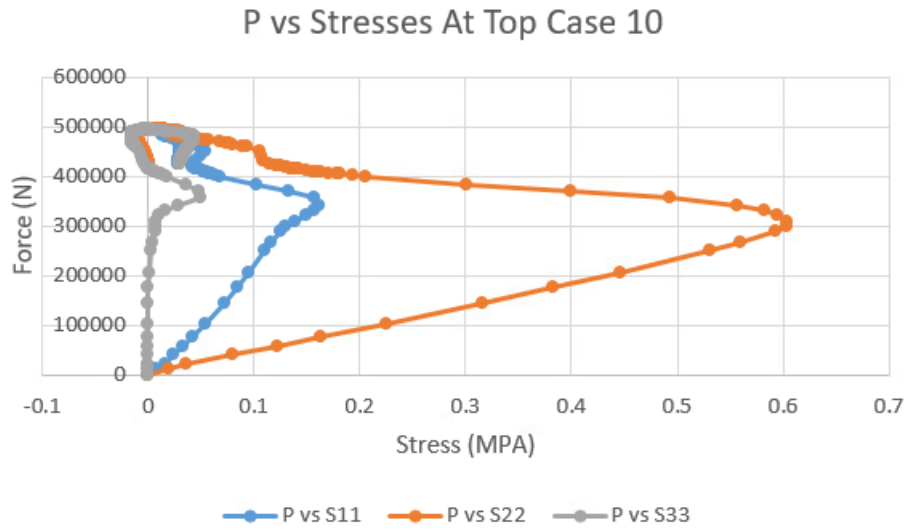


Figure 88 P vs S11, S22, S33 at Top of Wall for Case 10

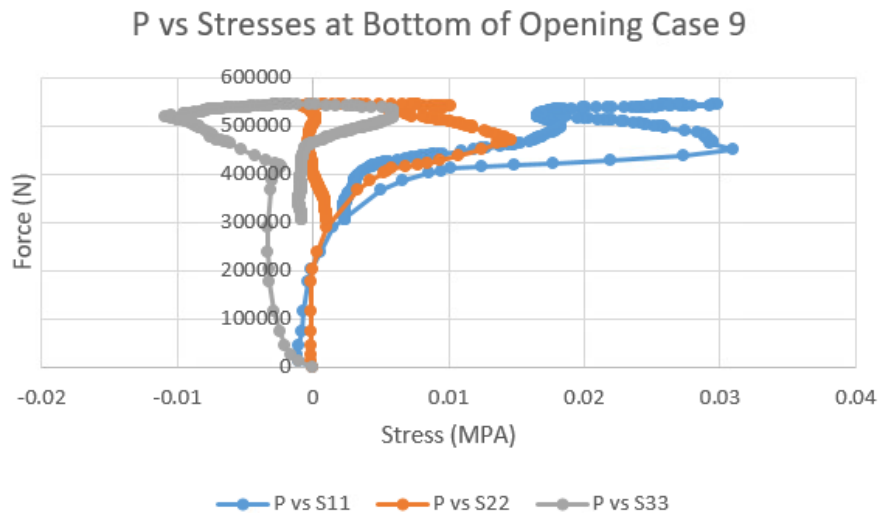


Figure 89 P vs S11, S22, S33 at Bottom of Opening for Case 9

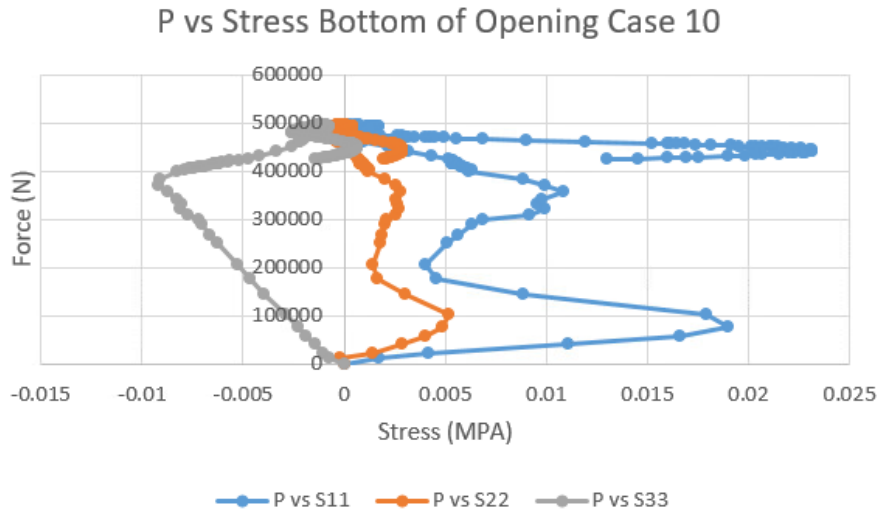


Figure 90 P vs S11, S22, S33 at Bottom of Opening for Case 10

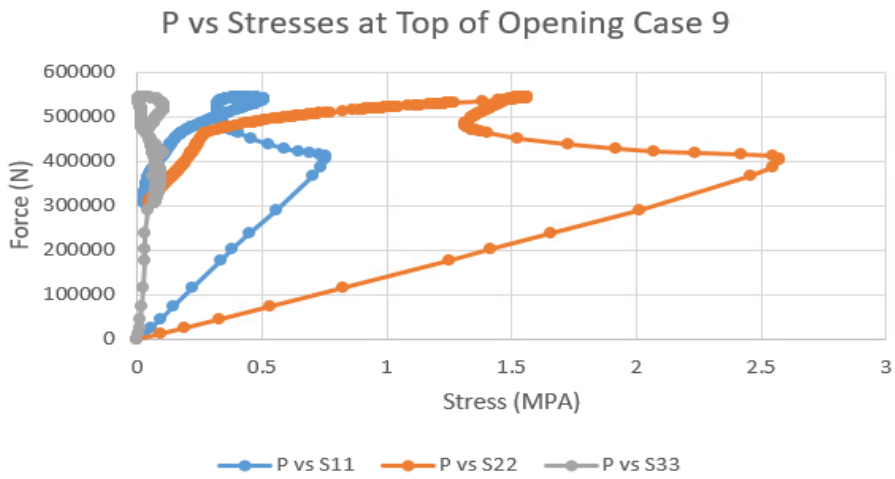


Figure 91 P vs S11, S22, S33 at Top of Opening for Case 9

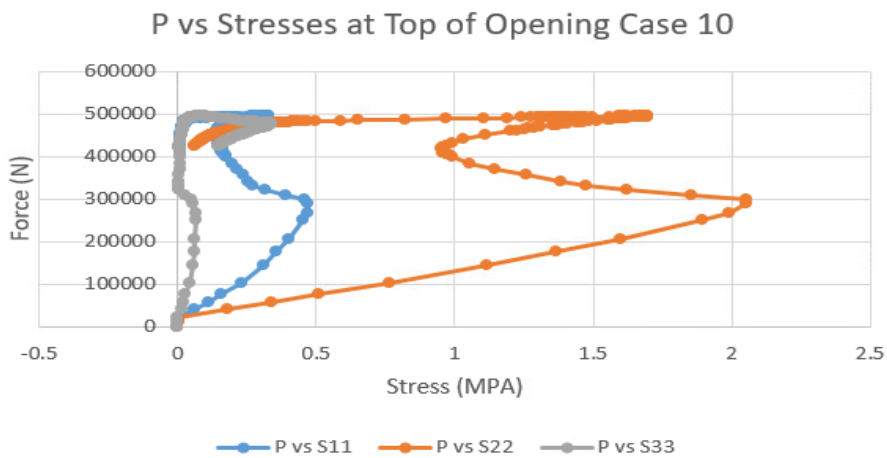


Figure 92 P vs S11, S22, S33 at Top of Opening for Case 10

It is shown that S22 has the most effect on the stress distribution as shown on the force displacement and force stress relations, except in the case where the selected node is at the bottom of the opening; however, this node shows enhancement in the force against stress where it shifted to the right. The smaller P vs S22 value at the top nodal surface of the wall compared to the top node of the opening is due to the stiffener's localized effect, which attracts and concentrates stress near the opening. While the load is applied uniformly at the top surface, the stiffener's presence causes a redistribution of stress, leading to a higher concentration of stress at the opening, particularly at its top node.

CHAPTER 5

SUMMARY, RECOMMENDATIONS, AND CONCLUSIONS

5.1. Summary

First, to validate the outputs of the software, simple linear elastic models such as fixed-fixed beams, ruler with point load on tip, beam column steel frame, column under axial load were modeled and compared with theoretical values. Then, 2 axisymmetric cylinders with and without caps, were modeled using different load and boundary conditions and yielded expected results. The CDP method was considered for rammed earth modeling structures (Chebeir, 2024)

As the validation of ABAQUS was done and the nonlinear method was chosen, more complex structures were modeled, such as walls with square openings, circular openings of different sizes and different locations, and with stiff material on openings.

The presence of openings significantly influences the stress distribution within the wall. As the size of the opening increases, the force-displacement curves at the top surface and the top of the opening converge closely. Meanwhile, the force-displacement response at the bottom of the opening diminishes, approaching zero for larger openings. When the opening is 40 cm by 40 cm or has a 40 cm diameter, the stress distribution shows dominance by S22, the in-plane stress in the loading direction. However, as the opening size increases to 60 cm by 60 cm and 80 cm by 80 cm, the out-of-plane stresses begin to dominate, particularly at the top and bottom edges of the openings, where they are consistently the primary stresses.

For a square opening of 40 cm by 40 cm or a circular opening with a 40 cm diameter at the center of the wall, the P- δ curve at the top nodal surface is more significant than at the top and bottom nodes of the opening. As the size of the opening

increases, the $P-\delta$ curve at the top of the opening begins to converge with the $P-\delta$ curve at the top nodal surface and may even surpass it if the opening size reaches 80 cm or more. Moreover, In the case of a 40 cm by 40 cm square opening or a 40 cm diameter opening, the $P-\delta$ curve at the top nodal surface is primarily influenced by in-plane vertical stresses, whereas at the opening, the $P-\delta$ curve is always dominated by transverse stresses in the x and z directions increase. The addition of a wood stiffener to the wall alters the stress distribution, enhancing the structural integrity and restoring the dominance of S22 across the wall, effectively mitigating the impact of larger openings on stress distribution.

5.2.Recommendations

Rammed Earth modeling requires several key areas:

- Investigate wind load effects
- Examine structural response to seismic loading.
- Analyze rammed earth material settlement, structural stability, and interaction with foundations
- Impact of temperature change on structural behavior
- Investigate creep effect over time
- Understand wall failure mode due to application of floor loads
- Assess different architectural opening effect on material failure.

5.3.Conclusions

Applying CDP nonlinear method to rammed earth walls allows engineers to gain insights into the material's structural performance and load-bearing capacity. By introducing openings of various sizes, the model illustrated how stresses are

distributed around these openings. Additionally, studying the behavior of stiffeners within these openings provided valuable information on how such reinforcements can effectively restrain the openings, aiding in the design of more resilient structures.

REFERENCES

- AlKareh, E. M. (2020). Rammed Earth Construction Development in Lebanon, *Master's Thesis*, American University of Beirut, Lebanon.
- ASTM, D. (2012). Standard test methods for laboratory compaction characteristics of soil using standard effort (12 400 ft-lbf/ft³ (600 kN-m/m³)). D698-12.
- Avila, F., Puertas, E., & Gallego, R. (2021). Characterization of the mechanical and physical properties of unstabilized rammed earth: A review. *Construction and Building Materials*, 270, 121435.
- Ávila, F., Puertas, E., & Gallego, R. (2022). Characterization of the mechanical and physical properties of stabilized rammed earth: A review. *Construction and Building Materials*, 325, 126693.
- Avrami, E.; Guillaud, H.; Hardy, M.; Terra literature review. An overview of research in earthen architecture conservation. *Los Angeles, The Getty Conservation Institute, 2008*
- Beer, F., Johnston, E., & DeWolf, J. (1999). Mechanics of materials, 5th SI Edition. *Stress*, 1(10), 1-12.
- Birnieks, L. (2013). Designing and Building with Compressed earth.
- Bui, T. T., Bui, Q. B., Limam, A., & Maximilien, S. (2014). Failure of rammed earth walls: From observations to quantifications. *Construction and Building Materials*, 51, 295-302.
- Bui, T. T., Bui, Q. B., Limam, A., & Morel, J. C. (2016). Modeling rammed earth wall using discrete element method. *Continuum Mechanics and Thermodynamics*, 28(1), 523-538.
- Burroughs, S. (2008). Soil property criteria for rammed earth stabilization. *Journal of Materials in Civil Engineering*, 20(3), 264-273.
- Chebeir, M. N. (2024). Testing, Validation, and Numerical Modeling of Rammed Earth Construction Materials, *Master's Thesis*, American University of Beirut, Lebanon
- Chen, J., Wang, Y., Shi, Q., Peng, X., & Zheng, J. (2021). An international comparison analysis of CO₂ emissions in the construction industry. *Sustainable Development*, 29(4), 754-767.
- Ciancio, D., & Beckett, C. (2013, January). Rammed earth: An overview of a sustainable construction material. In *3rd International Conference on Sustainable Construction Materials and Technologies, SCMT 2013* (pp. 1-9).

- Consoli, N. C., Silvano, L. W., Lotero, A., Scheuermann Filho, H. C., Moncaleano, C. J., & Cristelo, N. (2022). Key parameters establishing alkali activation effects on stabilized rammed earth. *Construction and Building Materials*, 345, 128299.
- El Nabouch, R., Bui, Q. B., Perrotin, P., Plé, O., & Plassiard, J. P. (2015). Numerical modeling of rammed earth constructions: analysis and recommendations. *Academic Journal of Civil Engineering*, 33(2), 72-79.
- Gramlich, A. N. (2013). A concise history of the use of the rammed earth building technique including information on methods of preservation, repair, and maintenance. *University of Oregon*.
- Jiang, M., Jiang, B., Lu, R., Chun, L., Xu, H., & Yi, G. (2023). Thermal and Humidity Performance Test of Rammed-Earth Dwellings in Northwest Sichuan during Summer and Winter. *Materials*, 16(18), 6283.
- Lee, J., & Fenves, G. L. (1998). Plastic-damage model for cyclic loading of concrete structures. *Journal of engineering mechanics*, 124(8), 892-900.
- Librici, C. (2016). Modelling of the seismic performance of a rammed earth building (*Doctoral dissertation, Universidade do Minho (Portugal)*).
- Lovec, V. B., Jovanović-Popović, M. Đ., & Živković, B. D. (2018). The thermal behavior of rammed earth wall in traditional house in Vojvodina: Thermal mass as a key element for thermal comfort. *Thermal Science*, 22(Suppl. 4), 1143-1155.
- Lubliner, J., Oliver, J., Oller, S., & Onate, E. (1989). A plastic-damage model for concrete. *International Journal of solids and structures*, 25(3), 299-326.
- Manual, A. S. U. S. (2012). ABAQUS 6.11. [http://130.149, 89\(2080\)](http://130.149.89(2080)), v6.
- Miccoli, L., Oliveira, D. V., Silva, R. A., Müller, U., & Schueremans, L. (2015). Static behaviour of rammed earth: experimental testing and finite element modelling. *Materials and Structures*, 48(10), 3443-3456.
- Nikishkov, G. P. (2004). Introduction to the finite element method. *University of Aizu*, 1-70.
- Nowamooz, H., & Chazallon, C. (2011). Finite element modelling of a rammed earth wall. *Construction and Building Materials*, 25(4), 2112-2121.
- Sarkar, S., Singh, I. V., & Mishra, B. K. (2022). A simple and efficient implementation of localizing gradient damage method in COMSOL for fracture simulation. *Engineering Fracture Mechanics*, 269, 108552.
- Silva, R. A. M., Oliveira, D. V., Schueremans, L., Lourenço, P. B., & Miranda, T. F. (2014). Modelling of the structural behaviour of rammed earth components.

Solan, D. G. (2019). Finite Element Modeling of Mechanically Stabilized Earth Walls Built with Welded Wire Wall Panels.

Wördenweber, B. (1984). Finite element mesh generation. *Computer-Aided Design*, 16(5), 285-291.